metals

MDPI

Article

Capacitor Electrical Discharge Sintering of Amorphous Fe-Si-B Powder

Rosa María Aranda [1,*], Petr Urban [2], Jesús Cintas [2], Juan Manuel Montes [2] and Francisco G. Cuevas [1]

[1] Department of Chemical Engineering, Physical Chemistry and Materials Science, Escuela Técnica Superior de Ingeniería, University of Huelva, Campus El Carmen, Avda. Tres de Marzo s/n, 21071 Huelva, Spain; fgcuevas@dqcm.uhu.es

[2] Department of Materials Science and Engineering, Escuela Técnica Superior de Ingeniería, University of Sevilla, Avda. de los Descubrimientos s/n, 41092 Sevilla, Spain; purban@us.es (P.U.); jcintas@us.es (J.C.); jmontes@us.es (J.M.M.)

* Correspondence: rosamaria.aranda@dqcm.uhu.es

Abstract

High purity powders of Fe, Si and B mixed with atomic composition $Fe_{78}Si_9B_{13}$ are subjected, after arc melting, to a melt spinning process. The amorphous ribbons are transformed into powder by mechanical milling, reaching mean sizes of 65 and 262 μm, taking care of maintaining the amorphous character. The powders are sintered by means of a very quick capacitor electrical discharge (CEDS), while trying to maintain the initial structure of the powders. The CEDS process is analyzed depending on the thermal energy applied during the discharge, as well as on the particle size of the powders and the powders' mass. The porosity, microstructure, hardness, electrical resistivity and magnetic properties of the prepared compacts are analyzed. Thus, for powders with a mean size of 262 μm, the porosity can be reduced from 0.33 to 0.11 after sintering, reaching a microhardness of up to 1100 HV_1 after applying a discharge of 2640 J/s. A coercivity of 1895 A/m and a saturation flux density of 1.32 T are achieved in the compact, which maintains a microstructure with up to 64% of amorphous phase.

Keywords: capacitor electrical discharge sintering; amorphous/nanocrystalline alloys; powder metallurgy; FAST; melt spinning; mechanical milling

1. Introduction

In the field of metallic materials, significant progress has been made during the last few decades in the knowledge of innovative alloys that can give rise to the so-called amorphous alloys or metallic glasses [1]. These materials, due to their strong predisposition to crystallizing, can only be produced with certain compositions and by means of special techniques that help to maintain their metastable microstructure. Some of these techniques process the material in a solid-state, such as the mechanical alloying of powders [2], obtaining a material without any structural order. Other techniques process by rapid cooling [3] the previously molten material, such as melt spinning or planar flow casting [4], laser glazing [5], suction casting [6], splat cooling [7] or additive manufacturing [8]. Materials obtained in this way retain the structure of the liquid itself, with some short-range ordering being common [9,10].

Whichever the obtention method, amorphous metals possess very attractive properties for structural and functional applications, such as high mechanical strength [11] and

Academic Editor: Nebojša Nikolić

Received: 14 January 2026
Revised: 12 February 2026
Accepted: 18 February 2026
Published: 21 February 2026

ductility [12,13], good magnetic properties [14], or wear and corrosion resistance [15,16]. In short, improved properties compared to their crystalline homologues.

Fe-based amorphous alloys have been the subject of intense research because of their lower fabrication costs as compared to other amorphous alloys, and at the same time they have excellent properties with wide application prospects and significant commercial value, mainly for magnetic applications. However, despite a general objective among metallic glasses, research is attempting to obtain bulk amorphous alloys [17], the moderate glass forming ability (GFA) [18] together with the high strength and brittleness of Fe-based metallic glasses, have meant that production is generally in the form of powders, ribbons, or in the best cases as wires and rods. Nevertheless, from 1995 onwards, Fe-based bulk metallic glasses were prepared by injection moulding in copper moulds or by flux melting and water quenching, resulting in relatively thick amorphous rods or plates [19,20].

An advantage of using powders, as compared, for instance, to ribbons, is the flexibility regarding the shape of the part to be manufactured. To this end, a first possibility is to mix these powders with polymers. However, the magnetic properties obtained for these mixtures worsen because the polymer occupies part of the piece space which does not behave positively [21]. In the case of using traditional powder metallurgy (PM) techniques [22], during sintering, a process that takes tens of minutes, the high temperature makes it difficult to control the unstable microstructures. For this reason, the development of techniques to reduce the time of permanence at high temperature, but ensuring an adequate joining between the powder particles, has been long pursued. One of these techniques is additive manufacturing [23–25]. Other methods look for the option of rapidly heating the material, which is an alternative to furnace sintering in PM traditional processes.

The electric current, passing through a resistive mass of powders, is an option to heat the material by the joule effect, causing micro-welds at the contact points between the particles. This is the working principle of the Field Assisted Sintering Techniques (FAST), with a variety of methods depending on the power source. Among the most used are spark plasma-assisted sintering (SPS) [26,27], induction sintering [28], electrical resistance sintering (ERS) [29–31] or capacitor electrical discharge sintering (CEDS) [32,33]; the latter two being ultra-fast processes with a current dwelling time of less than 1 s, which makes the use of protective atmospheres or a high vacuum unnecessary.

In this work, melt-spun amorphous Fe-Si-B ribbons were transformed into powder by mechanical milling in a disc mill [34]. The obtained powders were processed by CEDS by means of adapted commercial stud welding equipment, with special emphasis on controlling the crystallization of the material during processing. The high resistivity of the powders makes the current heat the particles' contacts by using the joule effect, softening these contact zones and, together with the applied mechanical load, inducing densification of the powders. This process is one of the variants of the process known as electrical discharge consolidation. As explained in [35], several other designations have been used to describe this or variants of this technique, including, among others, electric discharge sintering, electric discharge compaction, high-rate electric discharge compaction, environmental electric discharge sintering, capacitor discharge sintering and electric pulse sintering. Thus, capacitor discharge sintering [36], also known as electro sinter forging [37], consists of the combination of a single short impulse of intense electric current synchronized with a mechanical pulse, with energy being transferred after a predetermined level of pressure is reached. The main difference with CEDS is that the electrical pulse is generated by a high-voltage- and low-current capacitor bank in a primary circuit and then transformed in a secondary circuit to a high current–low voltage electro-magnetic discharge. Voltages in the primary circuit can reach values of about 1.5–3.5 kV, with voltages on the compacts ranging from 5 to 30 V [38]. This configuration limits the discharges and local plasma

formation during the process and can use switches based on power solid-state devices instead of ignitrons, increasing the reliability of the equipment. The electric pulse and application of pressure are synchronized to act together in the desired moment. A review of the actual use of this technique can be found in [39]. Moreover, controlled atmosphere devices have been developed [40], being the process usually called environmental electric discharge sintering.

In summary, the main objective of this work is to evaluate the feasibility of capacitor electrical discharge sintering (CEDS) as a consolidation technique for amorphous powders, while preserving their amorphous microstructure. The use of powders instead of ribbons is due to the greater flexibility in terms of the final shape of the consolidated parts, which is a key limitation of rapidly cooled amorphous ribbons. In this context, an amorphous Fe-Si-B alloy has been selected as a model material due to its known glass-forming ability [41] and its relevance for soft magnetic applications [42]. Although the optimization of magnetic properties is not the main objective of this study, the magnetic behaviour of the consolidated materials is evaluated as a functional indicator of the preservation of the amorphous microstructure during processing and as a reference for future process developments. Prepared compacts have been characterized by attending to their final porosity and level of sintering. Moreover, the microstructure is analyzed, and microhardness, electrical resistivity and magnetic properties are also determined.

2. Materials and Methods

Elemental iron (ATOMET 1001HP, purity > 99.4%, Rio Tinto, Montreal, QC, Canada), silicon (Amperit 170, purity > 99.6%, Flame Spray Technologies, Duiven, The Netherlands) and boron (Boron crystalline, purity > 98%, Alfa Aesar, Schwerte, Germany) powders were mixed to give the desired composition of $Fe_{78}Si_9B_{13}$ (a composition known as Metglas®, Metglas, Inc., Conway, SC, USA [43]). Batches of 7 g of powder were pressed at 450 MPa to obtain green compacts 8 mm in diameter, which were valid to be arc melted. The arc melting process (Edmund Bühler, MAM-1, Bodelshausen, Germany) was carried out in Ar atmosphere after Ti-gettering and repeated for 3 times to obtain a homogeneous alloy. Ribbons were obtained by melt spinning (Edmund Bühler, SC, Bodelshausen, Germany) under optimized conditions [44], which required using a rectangular nozzle of 0.4 mm × 10 mm at 1250 °C with a wheel surface speed of 28 m/s, a nozzle–wheel distance of 0.4 mm, and an ejection overpressure of 200 mbar.

The useful parts of the ribbons were then manually cut to pieces of about 10 mm and processed in a knives mill (Moulinex, MC3001, Lyon, France) for 3 min. Batches of 30 g of the sieved fraction lower than 5 mm were finally milled in a vibratory disc mill (Retsch, RS100, Haan, Germany) with a vibrating frequency of 50 Hz (making the disc to reach 700 rpm), and with a hardened steel disc and vial. After 30 or 120 min of milling, stopping for 5 min every 10 min to avoid excessive heating, two different powders with mean particle sizes of 262 or 65 μm were obtained, respectively [34].

Sintering of the amorphous powders was carried out by adapting commercial stud welding equipment (Thomas Welding, Nomark 10S, Jumet, Belgium), where the welding gun only maintained the switching function, being substituted, regarding the electric current conduction, by Cu electrodes (99.9% Cu–0.04% O) and thermal wafers (99.06% Cu, 0.760% Cr, 0.08% Zr, and 0.035% Ni) which also act as punches to press the powder particles (by means of a pneumatic press). The sintering assembly consisted of a 40 mm diameter sialon die with an inner orifice of 8 mm in diameter, closed by the Cu electrodes and the wafers (Figure 1).

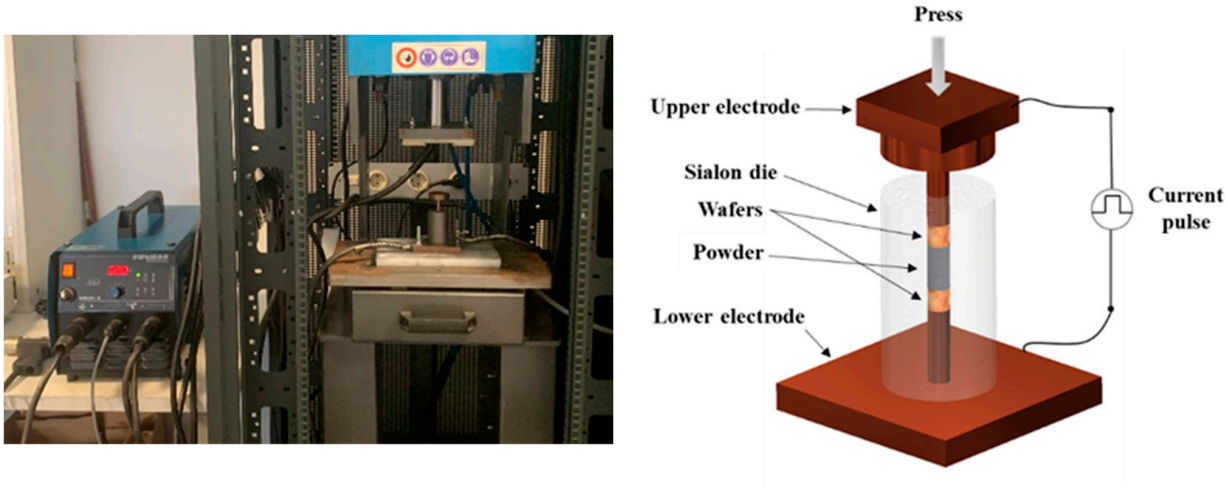

(**a**) (**b**)

Figure 1. (**a**) Stud welding equipment and pneumatic press used in the experiments. (**b**) Scheme of the sintering assembly, including electrodes and die, used in the CEDS experiments.

The experimental conditions included the use of 1 or 2 capacitors (1C or 2C, of 66 or 132 mF, which are the possibilities available in the stud welding equipment), and charging voltages of 125, 150, 175 and 200 V. Amounts of 0.75 g, 1.00 g or 1.25 g of amorphous powder were poured into the sialon die previously lubricated with graphite (deposited by means of an acetone suspension). The powder was then vibrated to accommodate the particles. A pressure of 200 MPa was applied using the pneumatic press, ensuring good contact between the electrodes and the powder column during the discharge process. At least four specimens were prepared for each processing condition.

The energy stored in the capacitors was then discharged over the amorphous powder column. The applied specific thermal energy (STE) can be calculated by Equation (1):

$$\mathrm{STE} = \frac{1}{\mathrm{M}} \cdot \frac{1}{2} \mathrm{CV}^2 \quad (1)$$

where M is the mass of the powder column, C the capacitance of the capacitor(s) and V the applied voltage. Moreover, the current passing through the powder column is monitored with the help of an oscilloscope, having measured a peak intensity of about 3.7 kA and a voltage of about 20 and 40 V when using 1C and 2C, respectively (Figure 2). It is expected that part of the energy dissipates in the equipment, therefore not reaching the powders. This effect can be calculated when the powder column resistance and the intensity passing through it are known. The comparison with the theoretical value resulting from Equation (1) reveals that the dissipation can reach up to 50%.

The actual composition of the melt-spun ribbons and the powders obtained by mechanical milling of the ribbons was determined using an electron probe microanalyzer (EPMA; Jeol, JXA-8200, Akishima, Tokyo, Japan), which allowed the comparison with the nominal composition of the alloy and the evaluation of the variations induced during milling.

X-ray diffraction (XRD) measurements were performed using Cu-Kα radiation (λ = 1.541 Å) on a Bruker D8 Advance A25 diffractometer (Bruker, Billerica, MA, USA). Two types of diffraction patterns were obtained: for quantitative Rietveld analysis, patterns were collected with a step size of 0.015° and a counting time of 0.5 s per step over a 2θ range of 30–80°; for qualitative characterization, patterns were acquired with a step size of 0.015° and a counting time of 0.1 s per step, over a 2θ range of 35–55°. The microstructure of the melt-spun ribbons, milled powders, and sintered compacts was examined by XRD and transmission electron microscopy (TEM; Philips, CM200, Amsterdam, The Netherlands) at

200 kV. For TEM studies, ribbons and compacts were prepared by a precision ion polishing system (PIPS; Gatan, 691, Pleasanton, CA, USA), and powders were directly observed in the microscope. Selected compacts were analyzed in detail by the Rietveld refinement method using TOPAS 3.3.0 (2020) software.

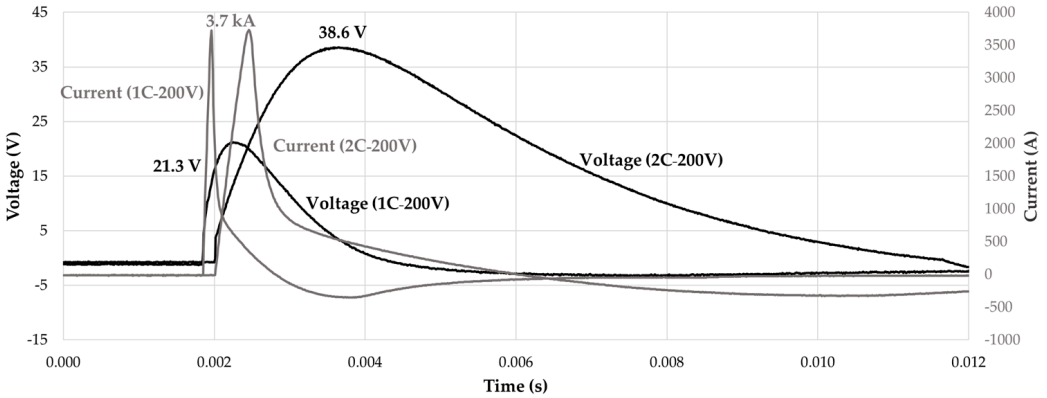

Figure 2. Representative electric current parameters measured when using 1 or 2 capacitors (66 or 132 mF) charged at 200 V, with a 1 g specimen.

The morphological study of the powders was carried out by means of high-resolution scanning electron microscopy (SEM; Thermo Fisher Scientific, FEI Teneo, Waltham, MA, USA). The particle size of the powders was determined by laser diffraction (Malvern Panalytical, Mastersizer 2000, Malvern, UK).

The thermal stability of the ribbons and powders was studied by differential scanning calorimetry (DSC; TA Instruments, 2010, New Castle, DE, USA) with a heating rate of 20 °C/min under Ar atmosphere.

Several properties were also determined: regarding the powders, the absolute density was measured with a pycnometer (Accupyc II 1340, Micromeritics, Norcross, GA, USA); Vickers microhardness $HV_{0.1}$ [45] of the ribbons was measured in their central and perimetral area (Shimadzu, HMV–G, Tokyo, Japan); and Vickers microhardness HV_1 in diametrical sections of resin-embedded sintered compacts, at the compact centre and each of the quadrant centres (Emcotest, DuraScan 50G5, Kuchl, Austria).

Furthermore, the hysteresis cycles of ribbons, powders and compacts were measured at room temperature with a vibrating sample magnetometer (KLA, MicroSense VSM EV9, Lowell, MA, USA) with a maximum applied field of 250 kA/m for the ribbons and 796 kA/m for powders and compacts, to determine the coercivity (Hc), the magnetic saturation (Bs or Ms) and the remanent flux density (Br).

In addition, the porosity of the sintered compacts was determined by weighing and measuring several specimens, and by Archimedes' method [46], and the porosity distribution (Nikon, Epiphot 200, Tokyo, Japan) was studied on diametrical sections of unetched specimens. The morphological characteristics of the fractures were studied on mechanically broken surfaces (after holding half compact and a sudden impact on the other half) by SEM.

A four-points probe and a Kelvin bridge (Chauvin Arnoux, CA 10, Paris, France) were used for the electrical resistance measurements at room temperature ($R_{measured}$). The thermoelectric effects were eliminated by changing the probes polarity in two different measurements, and the mean value was considered for each specimen. For the probe electrodes spacing (d = 1 mm), the electrical resistivity of the material can be calculated as indicated in Equation (2) [47]:

$$\rho = 2 \cdot \pi \cdot d \cdot R_{measured} \quad (2)$$

3. Results and Discussion

3.1. Amorphous Ribbons and Powders

The elemental composition of the melt-spun ribbons shows excellent agreement with the nominal values expected for the $Fe_{78}Si_9B_{13}$ alloy. The measured composition was 77.92 ± 0.30 at.% Fe, 8.81 ± 0.44 at.% Si and 12.54 ± 0.35 at.% B, together with 0.70 ± 0.09 at.% O and 0.04 ± 0.03 at.% Cu (mean values for 10 measurements with 20 μm × 20 μm analysis windows). The slight deviations observed are within acceptable limits and can be attributed to local segregations or effects associated with the high surface-to-volume ratio characteristic of melt spinning. The presence of traces of Cu is consistent with a possible transfer from the copper wheel used during processing, a phenomenon described in rapid solidification systems using Cu or Cu–Be wheels. On the other hand, the oxygen detected should not come from the processing, carried out under a protective argon atmosphere; its presence could be due to a subsequent slight surface oxidation, produced during storage or handling in ambient atmosphere, even under desiccation conditions, a typical behaviour in amorphous alloys rich in Fe and B due to their high surface reactivity [48].

Amorphous ribbons were obtained by melt-spinning, as confirmed by XRD and TEM. The optimum processing parameters determine the quality of the ribbons [49,50], yielding in our experiments to a process efficiency over 90%. This value refers to the fraction of the ribbon length that is morphologically and microstructurally homogeneous and completely amorphous, and therefore suitable for further experiments. The remaining 10% corresponds to the ends of the ribbon, which are normally discarded in non-continuous melt spinning processes due to unstable ejection conditions. Ribbons reached a microhardness of 936 ± 15 $HV_{0.1}$, with a coercivity of around 33 A/m. The coercivity value agrees with those found in the literature [51], with it being possible to reach even lower values after the proper heat treatment [52]. The improvement in magnetic properties after heat treatment is due to several factors, among which the following stand out: the relief of stresses generated during the amorphization process (by unblocking the walls of the magnetic domains), the creation of nanocrystals embedded in an amorphous matrix (which compensate the magnetocrystalline anisotropy between the crystalline and amorphous phases, of opposite sign, reducing the overall value) and the increase in electrical resistivity (due to the hindering of the movement of free electrons with the creation of the nanocrystals, which also leads to a decrease in losses due to Foucault currents) [53,54].

Powders obtained from the ribbons maintain the flake shape after 30 min, tending to be more rounded shapes after 120 min (Figure 3). Mean particle sizes of 262 ± 9 μm and 65 ± 8 μm were measured, respectively (nevertheless, these mean sizes should be considered with caution due to the flake shape of the powders and the measurement mechanism of the laser diffraction process).

To accurately assess the compositional changes induced by mechanical milling in air, the elemental composition of the powders milled for 30 and 120 min was quantified (10 measurements with 20 μm × 20 μm analysis windows). The composition measured for the powders milled for 30 min was 73.89 ± 2.51 at.% Fe, 8.22 ± 0.66 at.% Si, 9.64 ± 1.41 at.% B, 8.05 ± 2.01 at.% O, 0.08 ± 0.03 at.% Cr, 0.06 ± 0.02 at.% Mn, 0.04 ± 0.02 at.% Ni and 0.03 ± 0.02 at.% Cu, and for the powders milled for 120 min was 71.66 ± 3.89 at.% Fe, 7.55 ± 0.94 at.% Si, 10.23 ± 1.70 at.% B, 10.31 ± 4.16 at.% O, 0.08 ± 0.03 at.% Cr, 0.08 ± 0.02 at.% Mn, 0.06 ± 0.03 at.% Ni and 0.04 ± 0.02 at.% Cu. It showed an apparent decrease in the content of Fe, Si and B, and a progressive increase in oxygen, accompanied by traces of Cr, Mn, Ni, and Cu, with the new ones coming from the equipment wear. This compositional evolution is consistent with the mechanically induced oxidation of amorphous alloys described in the literature [55–57]. The continuous formation of new active

surfaces during particle fragmentation favours the surface nucleation of oxides (mainly SiO_2, B_2O_3 and Fe oxides), whose presence increases the total atomic fraction of oxygen, and apparently reduces the contents of Fe, Si and B.

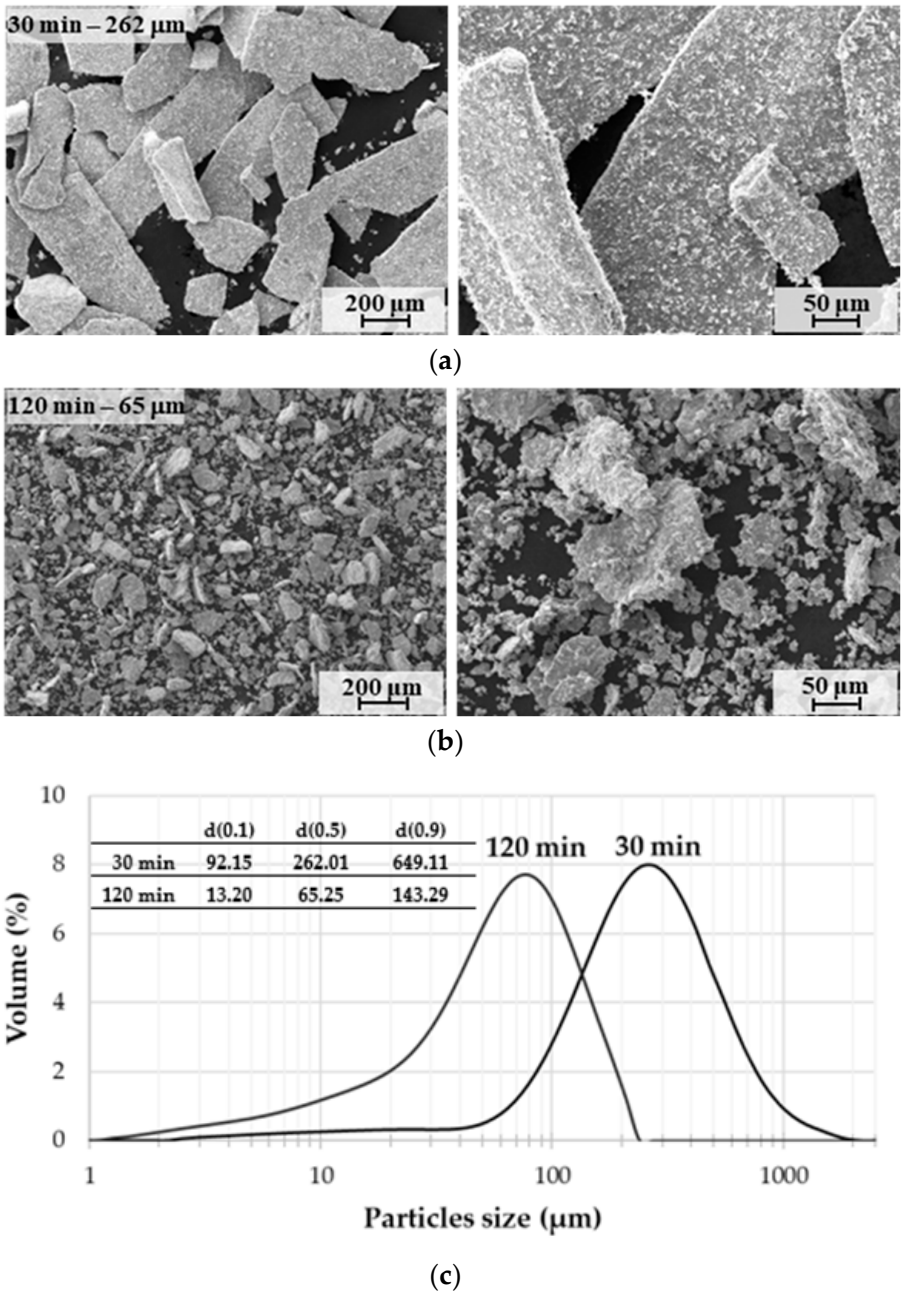

Figure 3. SEM micrographs of powders milled for (**a**) 30 and (**b**) 120 min, with mean particle sizes of 262 and 65 µm, respectively. (**c**) Powder particles size distribution and representative values.

Although this surface oxidation could be considered harmful, numerous studies indicate that it can play a functional role. Thus, a moderate oxygen content (8–10 at.% for short milling times) contributes to stabilizing the amorphous matrix, increasing the activation energy for crystallization, and delaying the formation of magnetically hard boride phases such as Fe_3B, Fe_2B, or FeB [54,58,59].

Conversely, classical studies, such as those by Trudeau et al. [60] indicated that the presence of oxygen during milling accelerates the crystallization kinetics in amorphous Fe-based alloys, but at the same time leads to the formation of significantly finer crystallites, which can be beneficial for magnetic properties. This behaviour is consistent with

recent works on mechanical crystallization [61] which points out that small amounts of finely dispersed oxides act as nanometric barriers that hinder the nucleation and growth of harmful intermetallics, favouring the formation of highly refined amorphous or nanocrystalline structures. However, both the classical literature and current reviews agree that a continuous or excessive supply of oxygen can excessively accelerate crystallization and modify the transformation routes, making it essential to control the atmosphere, grinding energy and operating mode to take advantage of the positive effects of oxygen without inducing premature crystallization or undesirable phases.

In this context, and according to the studies by Greer [62], the milling times used allow sufficient boron to be retained to maintain the amorphous stability. Likewise, the measured fractions of oxygen and wear elements remain within the ranges considered acceptable to avoid severe contamination that induces premature crystallization or the formation of extrinsic α-Fe particles, as warned by Bansal et al. [55].

Thus, short-term mechanical milling in air can provide a functional advantage: it allows the amount of surface oxides to be modulated and the inhibition of harmful boride phases, making it possible to obtain amorphous or fine nanocrystalline microstructures.

Figure 4 shows the XRD patterns of the ribbons and powders, with a broad peak characteristic of the amorphous state. Nevertheless, a slight increase in the peak height, higher for a longer milling time, could be due to the presence of a certain amount of α-Fe(Si) nanocrystals.

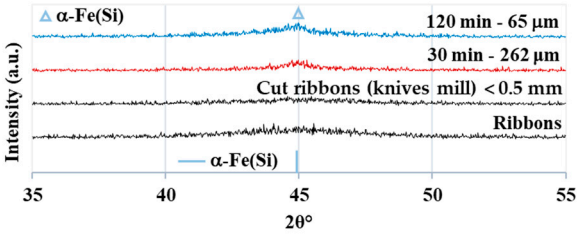

Figure 4. XRD patterns of $Fe_{78}Si_9B_{13}$ ribbons and powders after cutting the ribbons with the knives mill, and milled for 30 and 120 min. Also included are the positions of α-Fe(Si) peaks, according to ICCD (International Centre for Diffraction Data) PDF® (Powder Diffraction File™) card 00-006-0696.

The TEM study of the powders milled for 30 min reveals a predominantly amorphous microstructure (Figure 5a). For the powders milled for 120 min (Figure 5b), corresponding to a mean particle size d (0.5) of 65 µm, the microstructure remains mainly amorphous; however, a slightly higher presence of α-Fe(Si) nanocrystals is detected. High-resolution TEM (HRTEM) images allow the identification of both amorphous and nanocrystalline regions, where the nanocrystalline areas are indexed as α-Fe(Si), with lattice fringes corresponding to the (110) plane, and nanocrystals size of less than 5 nm. Fast Fourier Transform (FFT) analysis performed on selected regions further corroborates the presence of α-Fe(Si) nanocrystals embedded in an amorphous matrix.

It should be noted that the smallest particles (as those analyzed by TEM) are more transparent to the electron beam and therefore are easier to analyze; however, these particles may have experienced more severe milling conditions, potentially leading to a higher degree of crystallization than that of the powder as a whole.

Figure 6 shows the DSC results of the ribbons and the powders milled for 120 min. In both cases, a very smooth peak, corresponding to the primary crystallization of α-Fe(Si) is observed at temperatures around 400–500 °C, followed by peaks at temperatures of about 550 and 565 °C, of the crystallization of Fe_2B, Fe_3B, $Fe_{23}B_6$ or Fe_2Si [63–66]. These results show that the powders, even with prolonged milling times, remain mostly amorphous after milling, as already shown by XRD and TEM results.

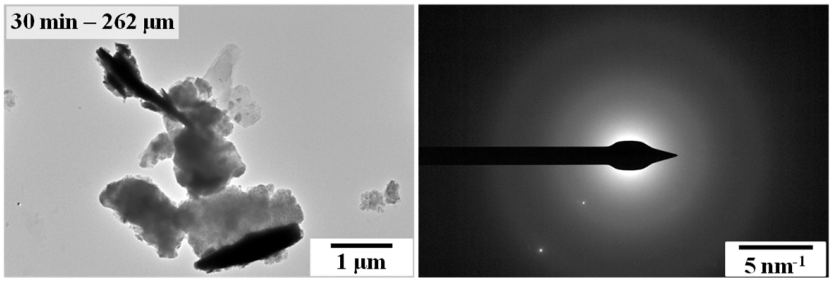

(**a**)

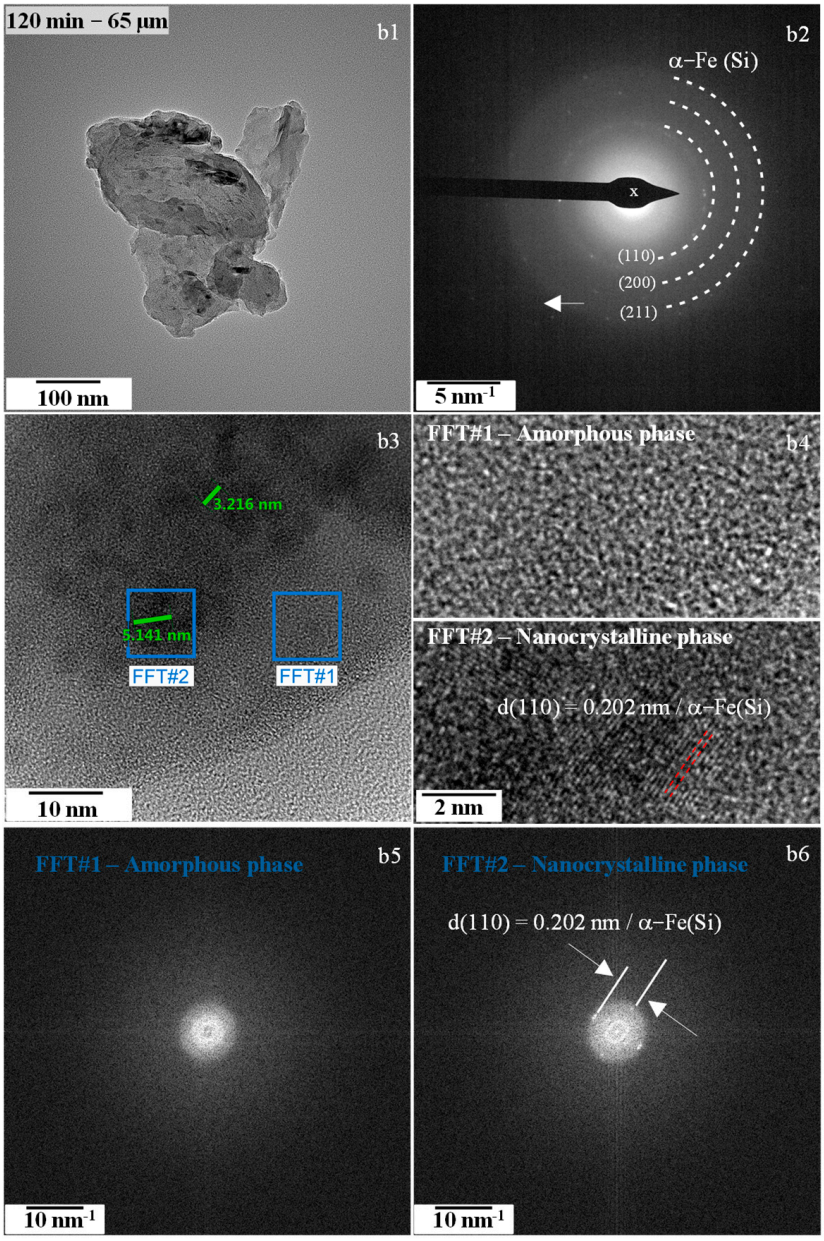

(**b**)

Figure 5. (**a**) TEM image and diffraction pattern of the $Fe_{78}Si_9B_{13}$ powders with particle size of 262 µm, (**b**) TEM and HRTEM images of $Fe_{78}Si_9B_{13}$ powders with particle sizes of 65 µm: (**b1**) TEM image of the powder; (**b2**) diffraction pattern with indexed planes of the α-Fe(Si) phase; (**b3**) HRTEM images showing the size of selected nanocrystals and the areas chosen for Fast Fourier Transform (FFT) analysis; (**b4**) HRTEM image showing amorphous and nanocrystalline areas; (**b5**,**b6**) FFT-derived diffraction patterns from the amorphous and nanocrystalline regions, respectively.

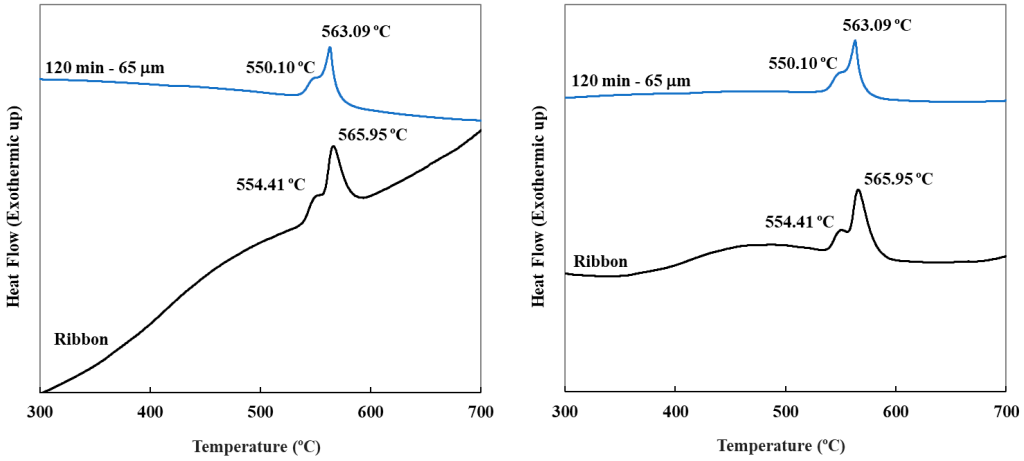

Figure 6. DSC analysis of the $Fe_{78}Si_9B_{13}$ amorphous ribbons, and 120 min milled powders. (**a**) Original results, the different slope is due to the relaxation of the powder during mechanical milling. (**b**) Results after baseline subtraction.

Regarding magnetic properties, as shown in Figure 7, the coercivity of the powders milled for 30 and 120 min is 3415 and 4008 A/m respectively. The remanent flux densities are respectively 0.035 and 0.034 T, and the saturation flux densities are 1.42 and 1.38 T.

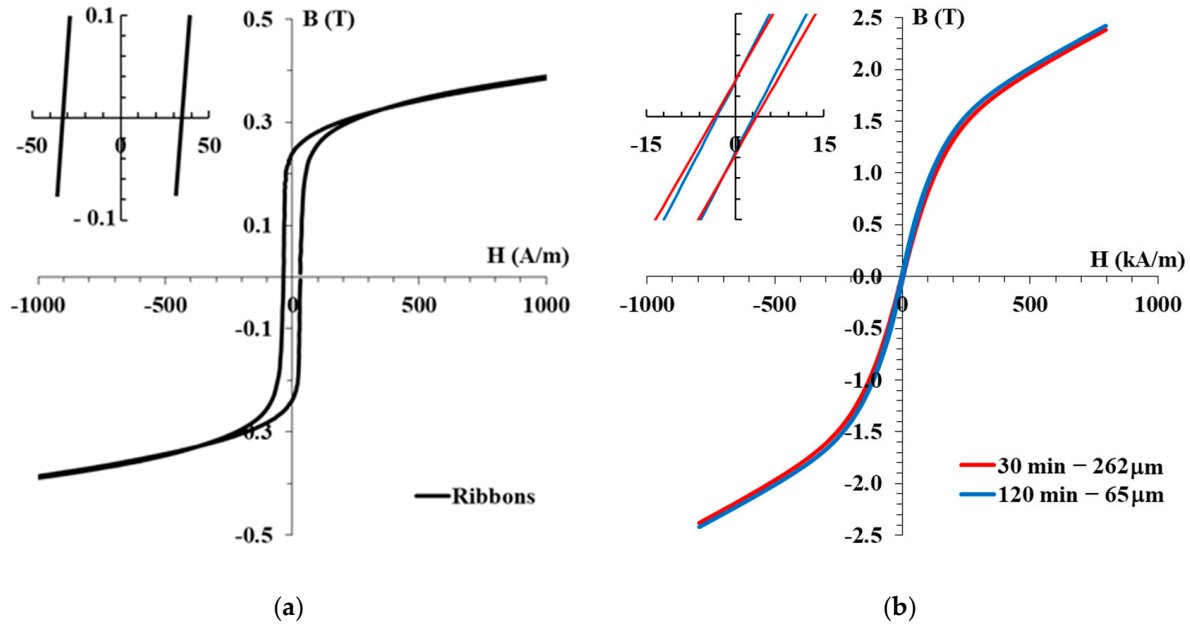

Figure 7. Hysteresis loops of (**a**) ribbons and (**b**) milled powders.

These magnetic properties are far from those obtained in the ribbons (coercivity, for example, was 33 A/m). The coercivities reported in the literature for amorphous powders obtained from ribbons vary inversely with particle size, while the remanent and saturation flux densities show a direct dependence. This behaviour could be due to the uncontrolled growth of nanocrystals by prolonging the milling process, although, in this work, XRD, TEM and DSC results suggest that the powders contain only a limited number of α-Fe(Si) nanocrystals. Thus, other causes, such as the internal stresses generated during the milling process, should be considered. In addition, the existence of air voids between the fine particles increases the internal demagnetising field and the coercivity increases [67].

Moreover, the coercivity can increase due to surface anisotropy, which can reach large values for small particles [68].

Results published on powders obtained by milling ribbons of $Fe_{78}Si_9B_{13}$, with sizes 25–75, 75–200 and 200–500 μm, showed coercivities of 3215, 1920 and 1341 A/m respectively [21]. The remanent flux density varied from 0.048 to 0.068 T, and the saturation flux density from 0.72 to 1.06 T. As explained by the authors, the high demagnetization value in the small particles, as well as structural defects induced during milling, could explain these values. The coercivity was reduced to 1240, 863 and 237 A/m after heat treating the powders at 500 °C for 1 h, probably because of proper nanocrystallization and the relaxation of internal stresses generated during milling.

These high coercivity values are not only observed after ribbons milling. Thus, mechanical alloyed $Co_{40}Fe_{22}Ta_8B_{30}$ powders, obtained after 200 h of milling and with an amorphous phase fraction of 96%, showed a coercivity of 3280 A/m, which was reduced to about 2000 A/m after heat treating [69]. According to the authors, this reduction is probably due to the relaxation of residual stresses and the elimination of free volume within the amorphous structure, which acts as a barrier to the movement of the magnetic domains. The reduction, however, can be limited because of the presence of B inclusions, surface anisotropy in the nanometre-sized particles, or anisotropy due to the surface roughness of the particles.

But not only the properties of powders can be affected by internal stresses, also those of ribbons [70,71] or those of amorphous materials obtained by electrodeposition can be affected [72]. It has been shown that these stresses depend on the side of the ribbon studied, being higher on the side in contact with the wheel than on the free surface [73]. Furthermore, the influence of external stresses applied to the ribbons, as those that could occur during milling, are evaluated on ribbons that are wound with different radii of curvature and to which different heat treatments are applied [74], concluding that compressive stresses are dominant in the properties presented by the material, as the coercivity, mainly affected by the movement of the magnetic domains.

Therefore, if magnetic properties are the objective, it could be interesting to start with powders with suitable properties, which are generally achieved with heat treatments allowing controlled nanocrystallization and stress relaxation. Nanocrystals smaller than 20 nm (the long-range ordering distances typical of crystalline structures) embedded in an amorphous matrix led to very satisfactory magnetic properties [75]. However, in this research, it is intended to use a powder with a high percentage of amorphous phase, to check the effect of the CEDS process on the microstructure, trying to avoid a high growth of the nanocrystals, as this causes a very detrimental effect on the magnetic properties.

3.2. Electrical Sintering of Amorphous Powders

3.2.1. Densification

The porosity Θ of the sintered compacts, measured by Archimedes' method, is studied as a function of the initial powders' size and the applied STE (Figure 8). The results obtained from the measurement and weighing of the compacts give slightly higher porosities, with a similar trend.

The porosity of the powder mass decreases after the sintering process, reaching lower values than the initial porosity of 0.33 for the coarse and 0.35 for the fine powders (these latter values measured after applying pressure before discharges, and measured based on sample dimensions and weight). Samples prepared with the small particles achieve higher densification, probably because of the higher number of contacts between particles. For instance, the 1.00 g compact sintered with 2 capacitors and 200 V (STE of 2640 J/g) reaches a porosity of 0.08 with the fine particles, but 0.11 with the big particles. With 0.75 g,

the same trend is observed, although somewhat higher porosities, above 0.1, are achieved despite the higher STE (3520 J/g); nevertheless, this is within the uncertainty interval of the measurements if compared with the 1.00 g mass. For a mass of 1.25 g, an increase in porosity does occur, with the minimum value remaining around 0.21, as expected when the STE decreases to 2112 J/g.

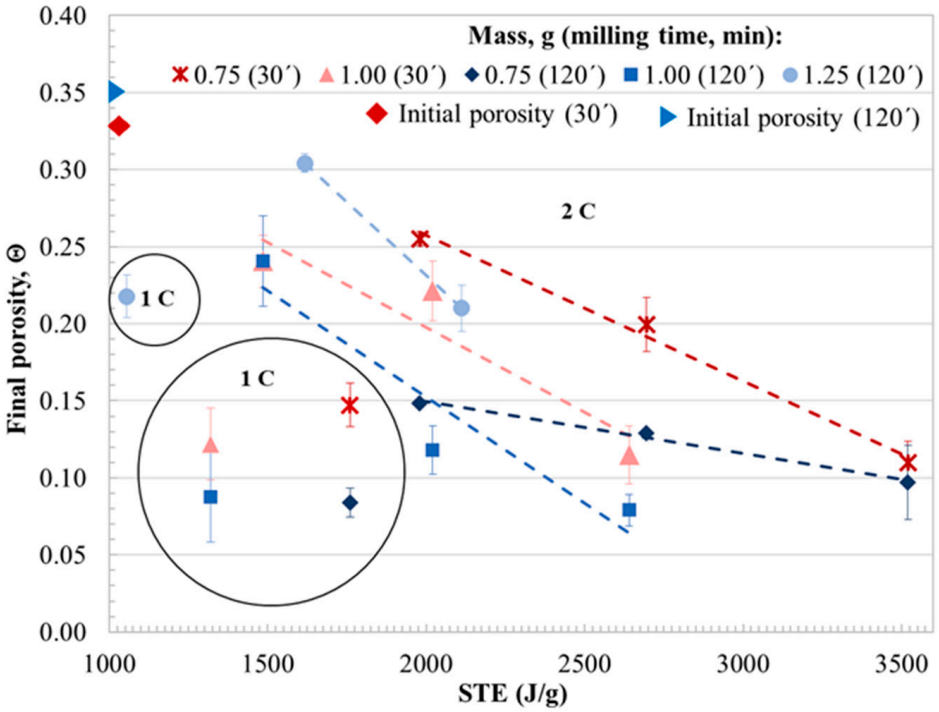

Figure 8. Porosity vs. STE of compacts prepared with powders milled for 30 and 120 min and sintered with 1 or 2 capacitors and different voltages (200 V for 1 capacitor, and 125, 150, 175 and 200 V for 2 capacitors) for 0.75, 1.00 and 1.25 g of powder. Dashed lines in the figure represent the trends.

On the other hand, sintering of the powders is not possible when 125 V is applied, and with certain conditions at 150 V the compact fractures during extraction. Furthermore, the effect of capacitance remains relatively minor. For instance, with powders milled for 120 min sintered at 200 V, the porosity decreases to 0.08 when using 2 capacitors, reaching a value of 0.09 with 1 capacitor, despite the discharge energy is half. For the powder milled 30 min, the porosity changes from 0.11 to 0.12. This implies that the energy supplied by 1 capacitor could be enough if the voltage is high enough, an observation that agrees with that of other researchers with respect to discharge sintering techniques, whereby even much higher voltages are used, with equipment specifically designed to carry out the process [32].

The study of the densification is completed with optical macrographs of diametrical sections of the compacts (Figure 9). Under certain low-energy discharge conditions, the compacts show a deficient consolidation in the lower central area, probably due to the preferential passage of the current through the periphery of the compacts. Areas with abundant porosity are also observed, due to the arbitrary path followed by the electric current. It is also observed that the powder milled for 120 min, and therefore with lower powder size, leads to lower porosities and best interparticle bonds. As a result, some compacts fabricated with a large particle size and low energy can break during the die extraction stage.

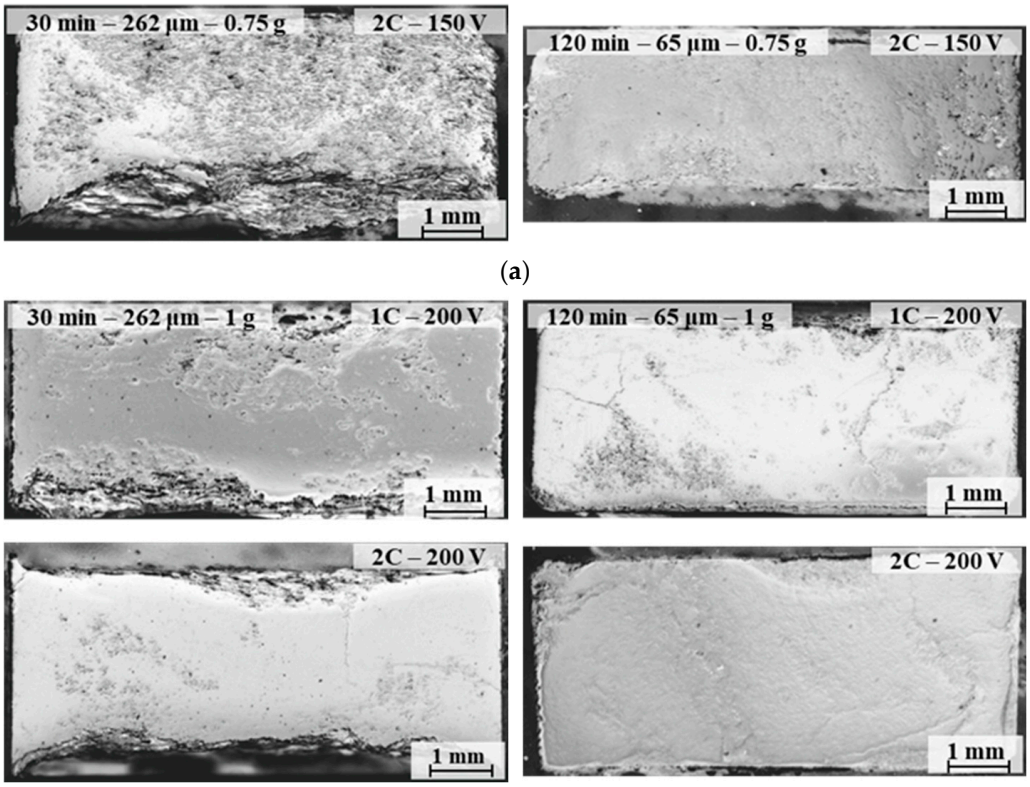

Figure 9. Optical macrographs of compacts fabricated under different conditions of voltage and capacitance, with powders milled for 30 and 120 min: (**a**) 0.75 g and 150 V, and (**b**) 1.00 g and 200 V.

Figure 10 shows details of the microstructure in one corner of the compact (left micrograph), and in the central area (centre and right micrographs), for compacts prepared with 1.00 g of powder. It is evident that the use of 200 V improves the densification and bonding between particles, and that the capacitance is less relevant. The sintering process is shown to be more effective as the particle size decreases, due to the higher resistivity and the consequent increase in energy generated by the electric current. The accommodation observed between particles of different sizes, a direct consequence of the vibration process before sintering, is also remarkable.

To conclude the study of the interparticle bonding, the fracture surfaces of compacts prepared with powder milled for 120 min were analyzed. Figure 11 shows that the use of 150 V generates few interparticle bonds, whereas the effect of sintering becomes clearer as the charging voltage increases. The difference between 66 and 132 mF is again difficult to appreciate, although in the first case the details at the fracture surface are finer.

These results are the consequence of three different main stages that have been defined for the electrical discharge consolidation processes [76]. In the first stage, with a duration of about tens of µs (as the other stages very much depend on the studied material and discharging parameters), resistance quickly decreases because of the electronic and later physical breakdown of any oxide layer surrounding powder particles, if present. Conducting layers are thus formed in the powder column. In the second stage, with about hundreds of µs in length, necks between powder particles are formed, even starting to grow. Current flows in longitudinal and radial directions, interconnecting powder particles and slowly decreasing the resistance of the powder column. In the third stage, with about tens of µs, again with a rapid drop of resistance, densification is promoted by the pinch forces from the centre to the periphery of the powder column. Additionally, a final, fourth stage takes place when elements from the atmosphere diffuse or are absorbed, leading to oxidation,

nitridation or carburization processes, which increase the resistance of the sintered powder column [77]. The effect of an externally applied pressure should be considered, if it is the case, in each one of these stages.

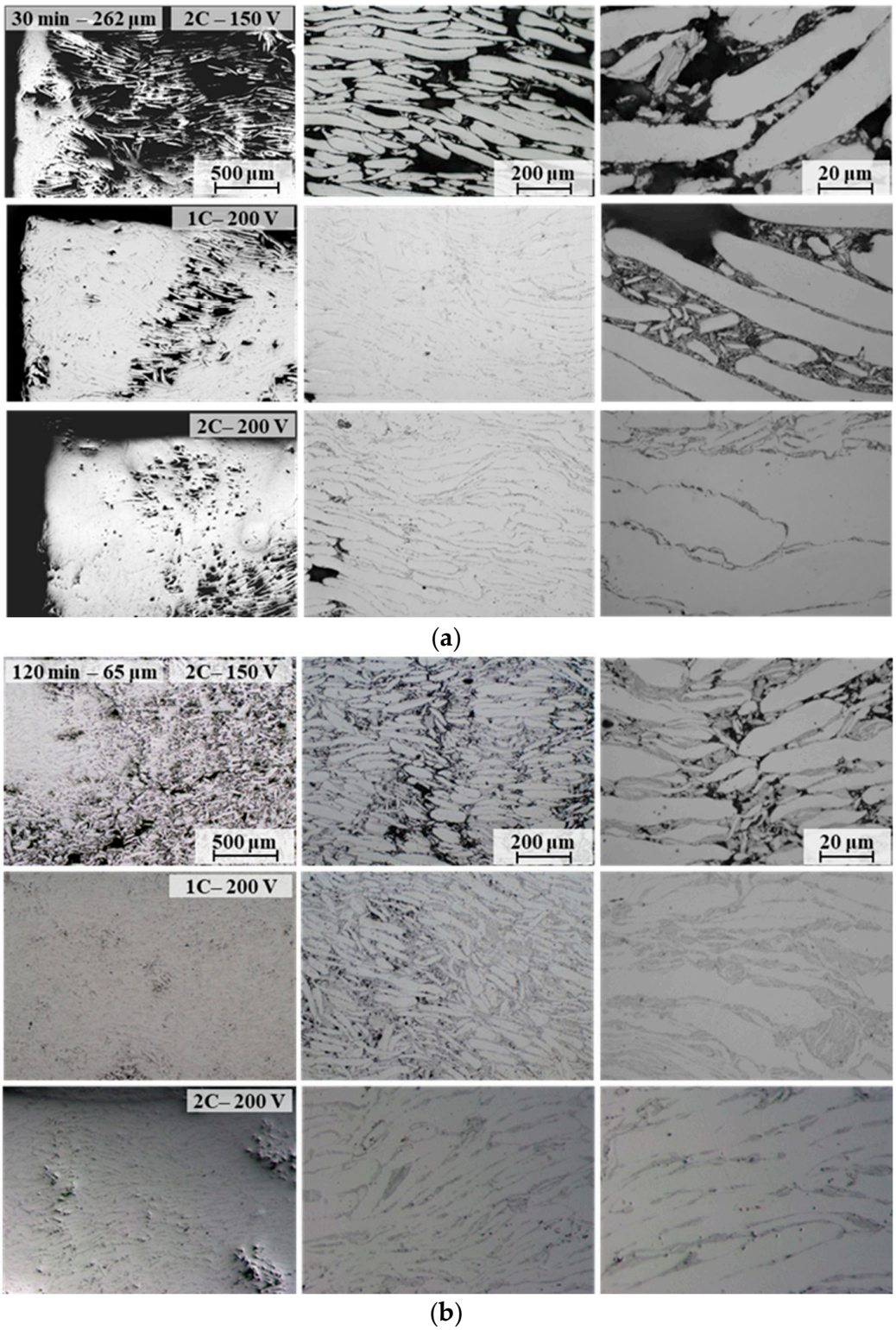

Figure 10. Optical micrographs of the 1.00 g compacts with an average powder size of: (**a**) 262 and (**b**) 65 µm, after discharge with 1 or 2 capacitors and voltages of 200 and 150 V. The electric current goes from the upper to the lower part of the images.

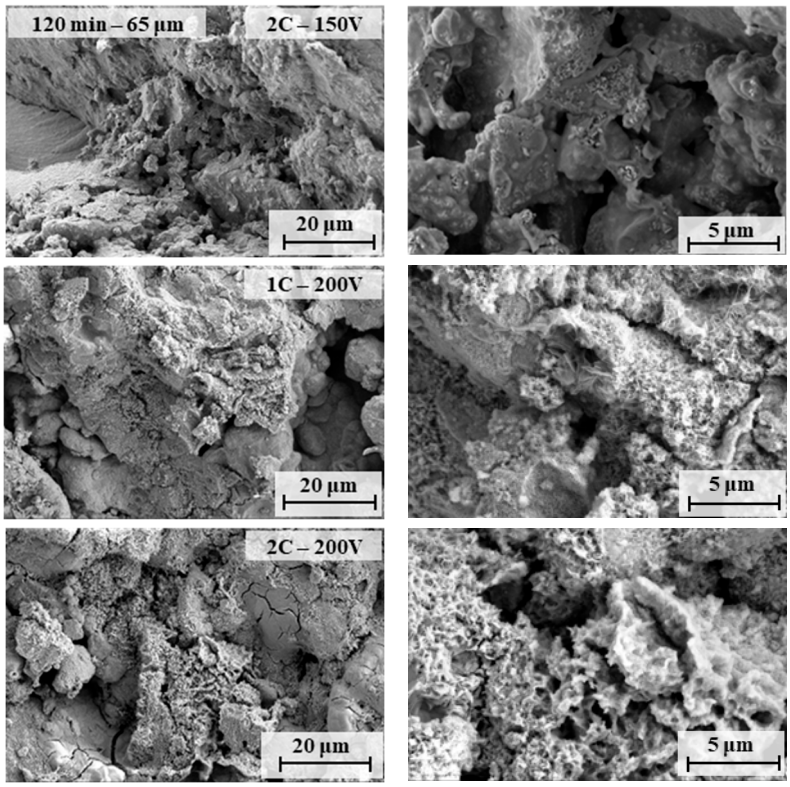

Figure 11. SEM micrographs of the fracture surface of 1.00 g compacts, prepared with powder milled for 120 min, sintered with voltages of 150 and 200 V, and 1 (66 mF) or 2 (132 mF) capacitors.

3.2.2. Microhardness

The Vickers microhardness (HV_1) of the different compacts is represented in Figure 12 versus the STE of the sintering process. An increase in microhardness is observed with the increase in the STE, because of the higher densification attained and the formation of better bonds between particles.

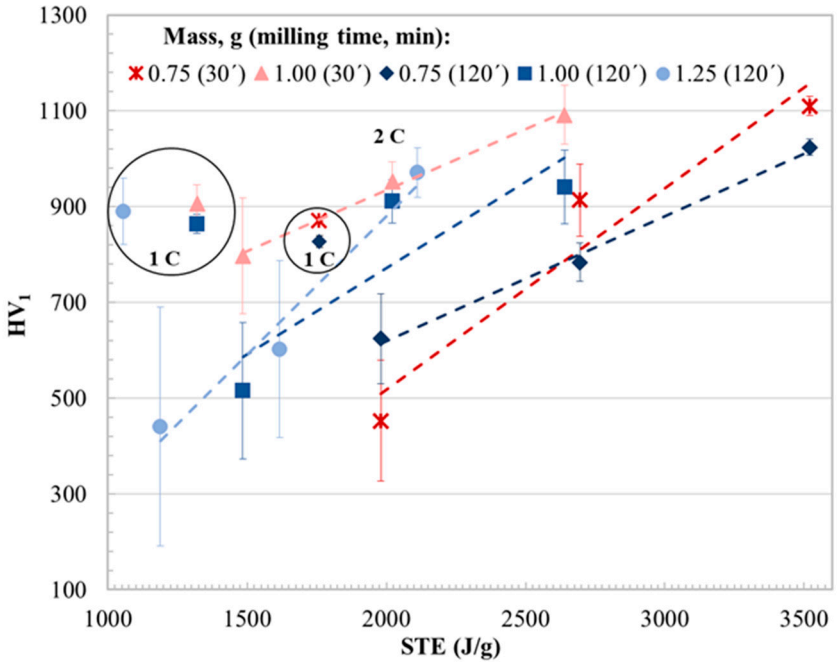

Figure 12. Microhardness HV_1 vs. STE of compacts prepared with powders milled for 30 and 120 min, sintered with 1 or 2 capacitors and different voltages, for 0.75, 1.00 and 1.25 g of powder.

Values between 900 and 1100 HV_1 are reached when sintering with 200 V and 2C (STE of 3520 and 2640 J/g for 0.75 and 1.00 g of powder respectively). These values are in the same order as that of the amorphous ribbon, with 936 $HV_{0.1}$. On the other hand, a lower STE (1188 J/g for 1.25 g sintered with 150 V and 2C), and the consequent higher porosity, causes the hardness to drop to values of 441 ± 250 HV_1, with a high deviation due to the greater inhomogeneity of the sintered compacts. Moreover, it is observed that capacitance has a clear effect on the hardness; for instance, values of 1091 ± 62 and 907 ± 39 HV_1 were measured for 1 and 2 capacitors, in both cases for compacts of 1.00 g prepared with powder of 262 μm and 200 V (2640 and 1320 J/g respectively). Despite the porosity values being similar (0.11 and 0.12), the bonds between the particles improved with increasing the STE.

3.2.3. Electrical Resistivity

The electrical resistivity of the compacts (Figure 13) has been measured as an alternative route to control the sintering process. A lower electrical resistivity is measured for a higher STE. The reason is the same as in the case of microhardness: increased densification and better bonds between particles. Some values show large standard deviations, mainly due to the differences between the two faces of the compact; however, when the densification is high, the deviation is negligible. The lowest resistivity, 7.97×10^{-7} Ω·m, is achieved with 1.00 g of 262 μm powder sintered with 2C and 200 V (STE of 2640 J/g), while the highest value, 3.31×10^{-5} Ω·m, is achieved with 1.00 g of 262 μm powder sintered with 2C and 150 V (STE of 1485 J/g). These values correspond to porosities of 0.12 and 0.24. For the porosity limits of 0.08 and 0.24, resistivities of 1.01×10^{-6} and 3.31×10^{-5} Ω·m are obtained; so, although there is a correlation between porosity and resistivity, other factors, such as the quality of the bonding between particles, must also be affecting the resistivity values.

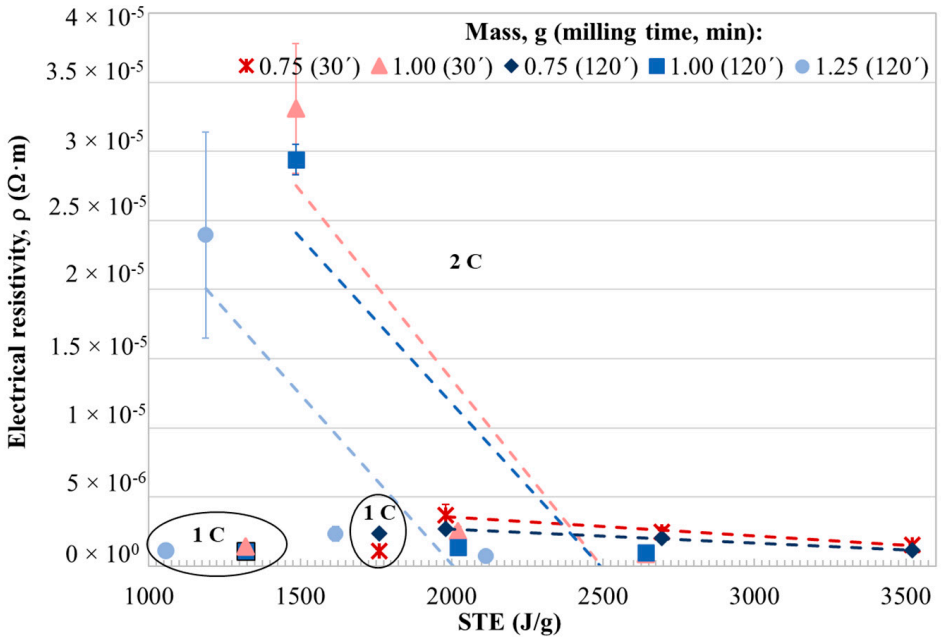

Figure 13. Electrical resistivity vs. STE of compacts prepared with powders milled for 30 and 120 min, sintered with 1 or 2 capacitors and different voltages, for 0.75, 1.00 and 1.25 g of powder.

3.2.4. Phase Analysis

Figure 14 shows the XRD patterns of the amorphous powder, and the compacts obtained with different conditions. According to the previously commented interparticle bonds, a considerable increase in temperature at the interparticle junctions must take place, and a certain crystallization corresponding to the appearance of α-Fe(Si) is observed despite

the extreme rapidity of the process. The presence of other phases cannot be discarded because of the coincidence of some of the diffraction peaks with those of the α-Fe(Si); nevertheless, these other phases should be present in small amounts. The crystallization is more pronounced for a lower initial powder size (since the starting point is a less amorphous powder) and for a higher STE, being again clear the higher influence of the voltage than that of the capacitance.

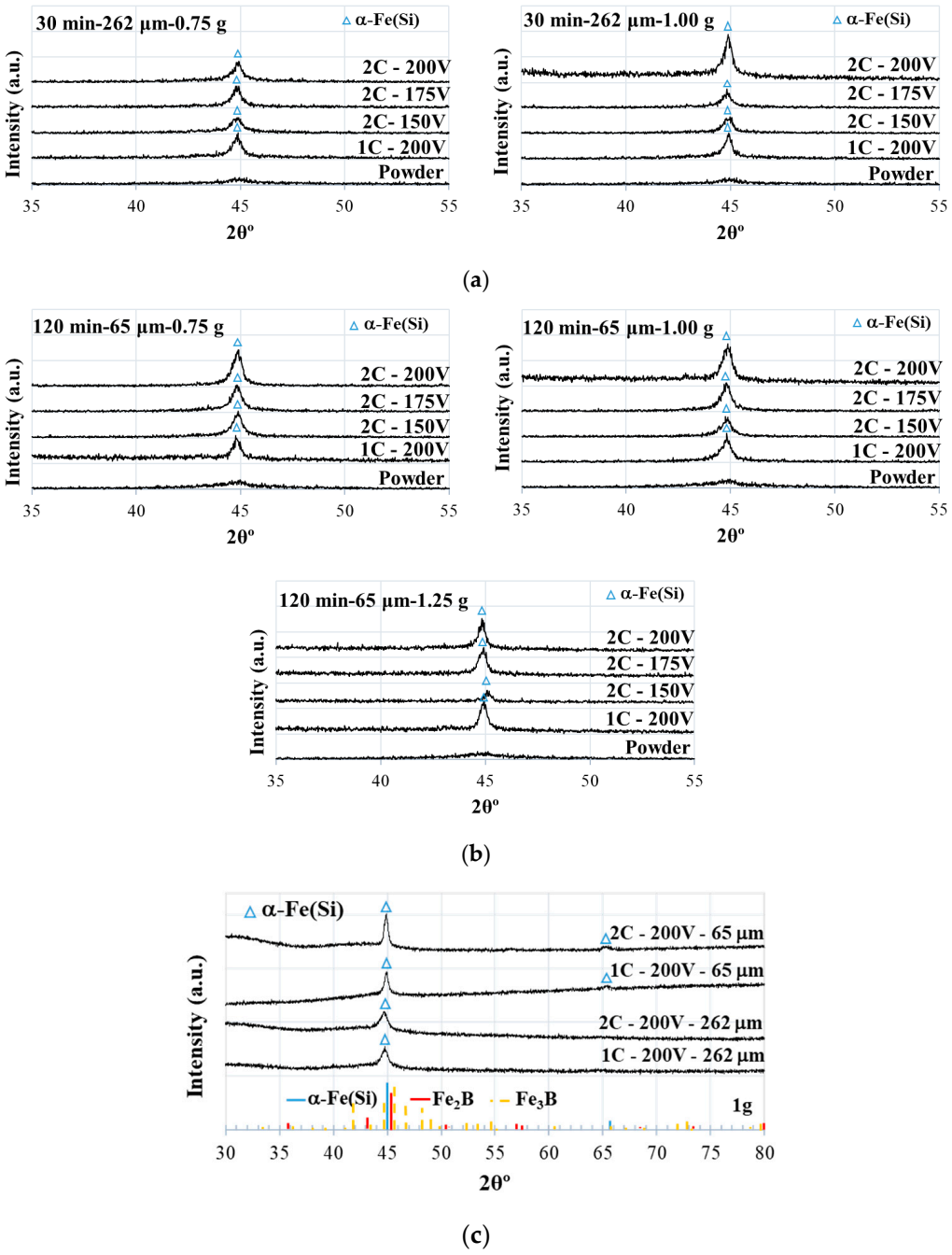

Figure 14. XRD patterns of the compacts obtained with 0.75, 1.00 and 1.25 g of powders milled for (**a**) 30 min and (**b**) 120 min. (**c**) Detailed XRD patterns of some of the compacts used for the quantitative phase analysis. Positions of α-Fe(Si), Fe_2B and Fe_3B peaks, according to the ICDD PDF cards 00-006-0696, 04-001-0965 and 04-001-3343, are also included.

The crystallization taking place, mainly of α-Fe(Si) particles, and the resulting crystal size are calculated by the Rietveld method for the compacts of 1.00 g sintered with 200 V and the use of 1 or 2 capacitors, with the two different powder sizes (Table 1).

Table 1. Results of the XRD analysis using the Rietveld method.

Milling Time	Capacitance (mF)	Crystallite Size (nm)	Crystallinity (%)
30 min	1C (66)	6.8	30.1
	2C (132)	6.1	35.8
120 min	1C (66)	22.3	51.4
	2C (132)	23.4	59.2

In all cases, the crystallite size of the α-Fe(Si) particles remains below 25 nm, and with the powder of 262 μm (30 min of milling time) is as low as about 7 nm. On the other hand, the crystallinity values, although calculated with very low error (R_{brag} < 0.28), are not entirely reliable because of certain fluorescence noise overlapping with the signal of the samples, but the trend can be shown. The amorphous phase in the consolidated samples remains in values of 65–70%, although this value is clearly reduced to 40–50% for the smaller powders consolidated under more energetic conditions.

To complete the microstructural study, the same compacts were studied by TEM (Figure 15a,b). The compacts obtained from the powder milled for 30 min (mean particle size of 262 μm) retain an amorphous matrix with nanocrystals smaller than 40 nm, whereas the crystallite size in the compacts prepared with the powder milled for 120 min (mean particle size of 65 μm) reaches 75 nm. The presence of the amorphous matrix agrees with that observed by XRD, although the crystallite sizes measured with TEM are higher. This discrepancy can be due to the intrinsic limitations of the XRD line-broadening-based methods when amorphous halos and nanocrystalline peaks overlap. As happened in XRD, the presence of small amounts of other phases, such as Fe_2B, Fe_3Si and Fe_3B, cannot be discarded.

Moreover, a high-resolution TEM image of the compacts prepared with the 120 min milled powder has been included (Figure 15b), showing nanocrystal with sizes under 75 nm (see measurement in the micrograph), as also observed near the edge of the TEM images. These observations are consistent with the Rietveld quantification, which revealed a volume-weighted average nanocrystal size slightly above 20 nm. This difference is explained by the size distribution of nanocrystals observed in the TEM analysis, confirming the coherence between direct imaging and quantitative diffraction measurements.

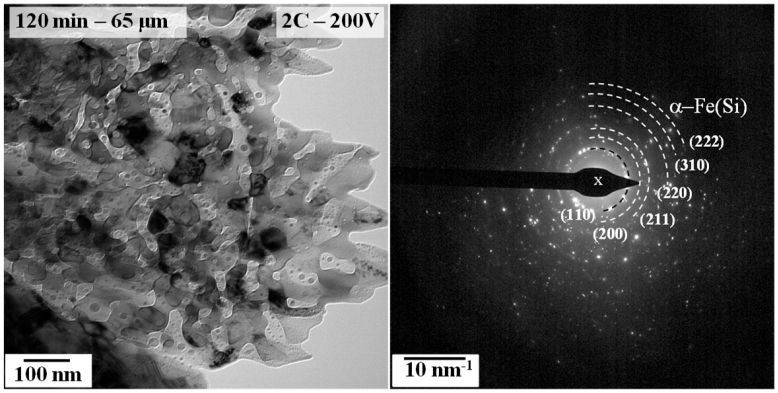

(**a**)

Figure 15. *Cont.*

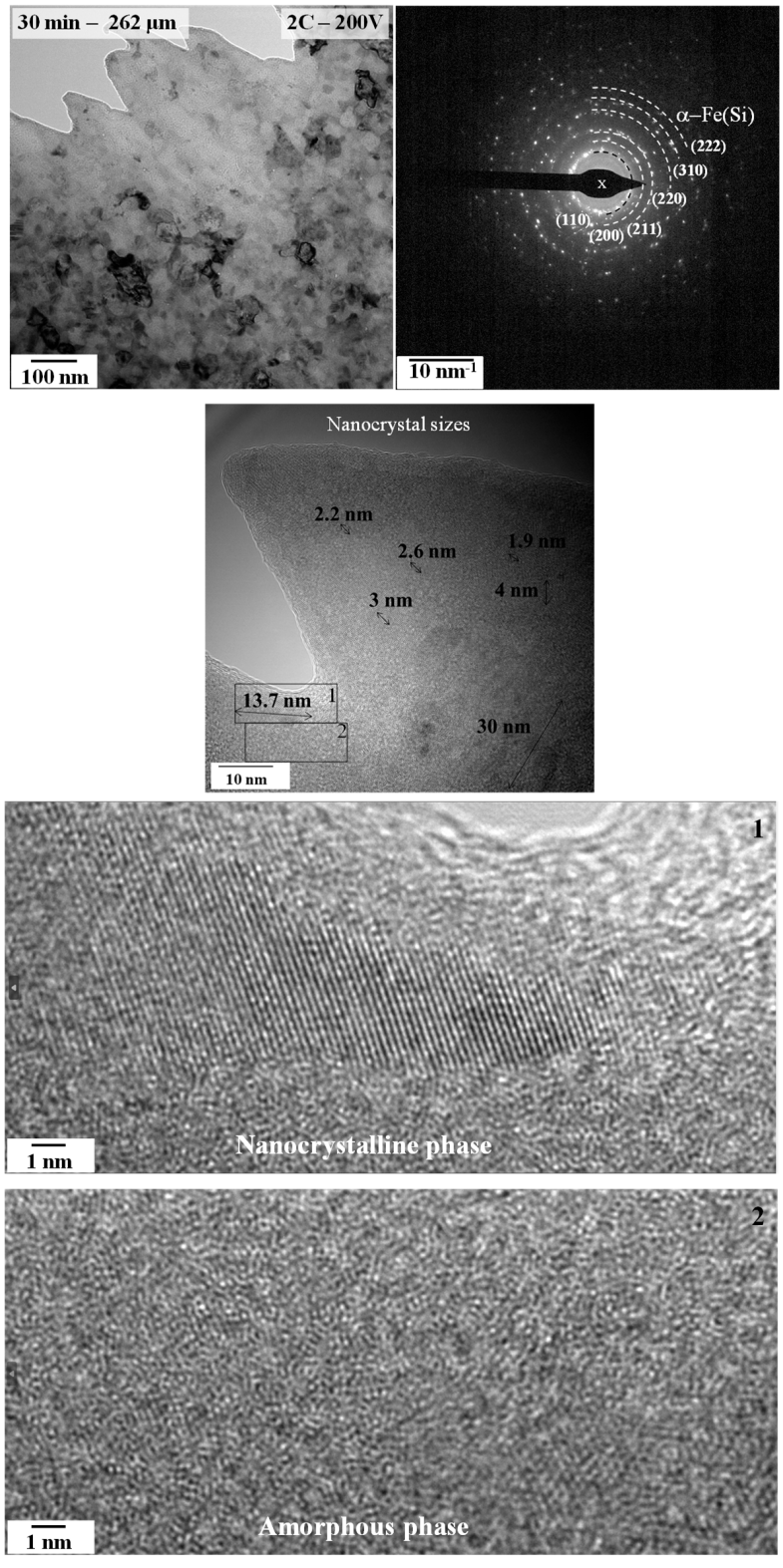

(**b**)

Figure 15. TEM micrographs and diffraction patterns of the central zones of compacts sintered with 2C and 200 V, with powder of milled for (**a**) 30 min and (**b**) 120 min.

Thus, the combined XRD and TEM results indicate that the CEDS process induces a partial nanocrystallization of the amorphous Fe–Si–B powders while preserving a significant fraction of the amorphous matrix. The resulting microstructure can therefore be described as amorphous–nanocrystalline, with the volume fraction and size of the crys-

talline phase being strongly dependent on the powder milling history and the sintering energy input.

3.2.5. Magnetic Properties

The magnetic behaviour is discussed considering the combined effects of powder particle size, milling time and CEDS processing parameters. Figure 16 shows the hysteresis cycles of some of the sintered compacts. Larger initial particles (powder milled for only 30 min) lead, in general, to lower values of coercivity, remanent, and saturation flux densities than those measured in the powders. For instance, after sintering 1.00 g of powder with 2C–200 V, the coercivity decreases from 3415 in the powders to 1895 A/m, the remanent flux density from 0.036 to 0.028 T and the saturation flux density from 1.42 to 1.32 T. However, it is not possible to reduce the coercivity for compacts made with powder milled for 120 min, increasing from 4008 A/m in the powders to values between 4122 and 4841 A/m. Similarly, the remanent flux density changes from 0.034 T to values between 0.052 and 0.063 T in the compacts, and the saturation flux density from 1.38 T to values between 1.34 and 1.39 T.

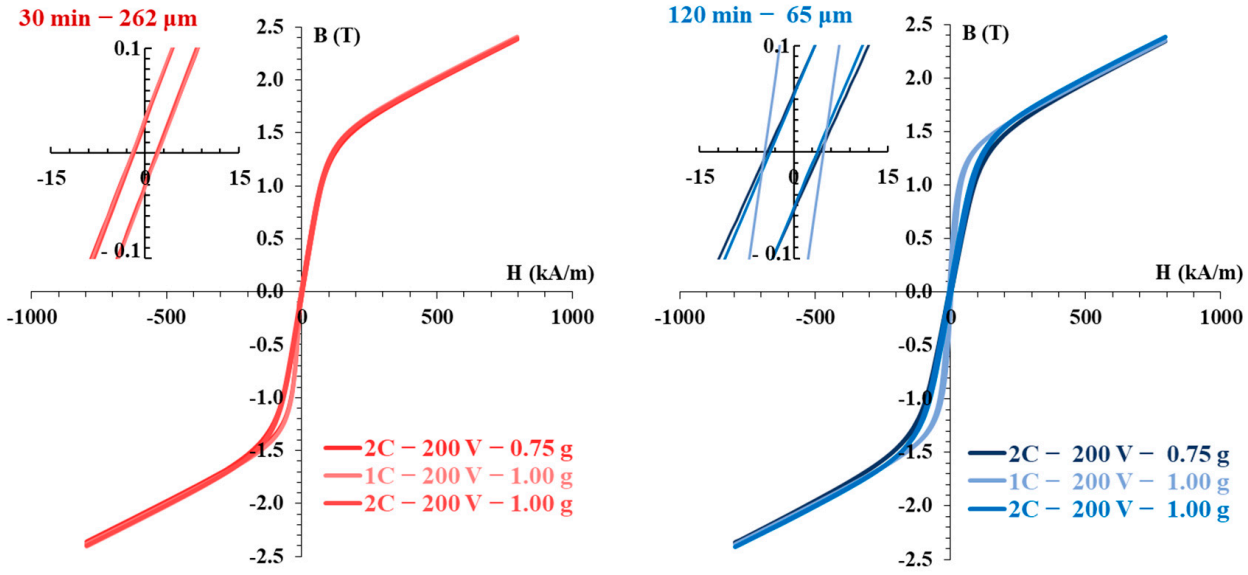

(**a**) (**b**)

	30 min – 262 µm			120 min – 65 µm		
	Hc (A/m)	**Bs, Ms (T, emu/g)**	**Br (T)**	**Hc (A/m)**	**Bs, Ms (T, emu/g)**	**Br (T)**
Powder	3415	1.42, 163.81	0.035	4008	1.38, 162.92	0.034
2C – 0.75 g	2202.71	1.28, 170.60	0.033	4695.87	1.39, 177.23	0.060
1C – 1.00 g	2264.78	1.41, 170.77	0.036	4840.70	1.36, 167.99	0.063
2C – 1.00 g	1894.74	1.32, 170.86	0.028	4122.11	1.34, 172.13	0.052

(**c**)

Figure 16. Hysteresis cycle of 0.75 and 1.00 g compacts sintered with 200 V and 1 or 2 capacitors, from powder of (**a**) 30 min—262 µm and (**b**) 120 min—65 µm. (**c**) Magnetic properties of powders and compacts.

This behaviour evidences the competing mechanisms governing the magnetic response. These values of the coercivity are probably a result of the equilibrium between the improvement of the magnetic properties due to the particles' boundaries blurring after sintering, the deterioration of the magnetic properties due to crystallization, mainly with crys-

tals above the optimal size of 20 nm (which can also reach 100 nm for certain materials [54]), and the influence of the distance among nanocrystals within the amorphous matrix.

Moreover, pronounced micro stresses, generated during the mechanical milling of the ribbons, microstructural defects, and even the possible appearance of detrimental phases such as Fe_2B, Fe_3Si and Fe_3B, which act to increase the magnetocrystalline anisotropy and to fix the magnetic domains, should be avoided to improve the magnetic properties [78]. These same phenomena, together with the possible stresses generated during sintering, act to decrease the saturation and remanence, by an increase in the magnetoelastic coupling that results in the irreversible rotation of narrow domains in the magnetization curve [79].

Probably, as XRD and TEM showed, the nanocrystallization produced after ribbon milling and CEDS, the defects and micro stresses generated in the compacts, as well as the presence of porosity, cause the magnetic hardening of the material. However, the measured values are not very different from those obtained with similar processing techniques. Thus, compacts obtained by SPS [80,81] of amorphous Finemet powders, obtained after 30 h of mechanical alloying, showed a saturation magnetization of 132.3 emu/g (with a coercivity of 5928.5 A/m), whereas for compacts prepared with powder milled for 120 h, the saturation increases to 166.8 emu/g (with a coercivity of 8689.8 A/m). The increased presence of the Fe_3Si phase, the grain refinement and a crystals distribution more homogeneous after 120 h, lead to a reduction in the magnetocrystalline anisotropy, facilitating the movement of the magnetic domain walls, which results in the increase in the saturation magnetization. These saturation values are similar to those obtained in the compacts of our research (highest value of 177 emu/g), but the coercivities are quite higher (values of our research between 4841 A/m and 1895 A/m), mainly due to the presence of a high volume of nanocrystals of the Fe_3Si phase, which produce an increase in magnetostriction and consequently an increase in coercivity. Even higher coercivities, of up to 9024 A/m were measured for Fe-Si-B compacts obtained with powders milled during 90 h. The lower coercivities obtained in our research suggests that, as described above, the CEDS process seems to largely preserve the starting structure, while achieving a good bonding between particles, leading to a nanocrystallization not far from the optimal value of 20 nm.

In a different study, amorphous atomized powders of Fe-Si-B-P-Cu were consolidated by SPS [27], showing a saturation magnetization that gradually increased from 148 to 161.8 emu/g by increasing the sintering temperature from 389 to 439 °C. According to the authors, this raise was caused by a higher amount of small α- Fe crystals (with sizes below 20 nm) and a more homogeneous distribution of the amorphous and crystalline phases (the closer the magnetic domains are, the easier the exchange between domains and the better the magnetic properties of the material). Increasing the sintering temperature up to 482 °C leads to a slight decrease in the saturation magnetization until 154.1 emu/g, mainly due to the crystals growth above 20 nm and the precipitation of Fe(B,P) compounds that caused the anchoring of the magnetic domains. Moreover, sintering at 389, 439 and 482 °C makes coercivity first decrease from 217 to 180 A/m, and then to increase to 271 A/m, due to factors such as the nanocrystals size and the presence of defects at the micro- and macroscopic scale, such as internal stresses and porosity. Nevertheless, these relatively good results can be due to an annealing treatment carried out under very high pressures, around 800 MPa, obtaining highly densified nanocrystalline compacts with few defects.

Finally, compacts prepared with amorphous Fe-Si-B powders [82], obtained from ribbons milled in a planetary ball mill at a low temperature, and consolidated at ultra-high pressure of 5.5 GPa for 3 min in a hydroforming machine, up to densities of 97.8%, resulted in an amorphous matrix with nanocrystals of about 19 nm. The measured coercivity was of about 285 A/m. This value is higher than that obtained in the ribbons, according to the

authors, because of the presence of residual porosity in the parts and due to internal stresses and defects appearing during mechanical alloying and consolidation. This prevents the movement of the magnetic domains. Thus, a heat treatment of the consolidated parts for 30 min at 300 °C reduced the coercivity to 118 A/m, and to 83 A/m if performed at 400 °C, highlighting the key role of controlled crystallization and stress relaxation.

For completeness, the magnetic properties obtained in this work are also compared with those of conventional soft magnetic materials. Typical non-amorphous soft magnets, such as sintered Fe–Si steels, exhibit saturation magnetization values in the range of 200–220 emu/g and coercivities typically below 100 A/m, while ferrites show much lower saturation magnetization (60–80 emu/g) combined with very low coercivities. In comparison, the compacts produced in this work present intermediate saturation magnetization values (up to ~177 emu/g) and higher coercivities, which is expected considering the presence of residual porosity, internal stresses, and, probably, uncontrolled partial nanocrystallization inherent to these powder-based consolidation routes.

It should be emphasized that conventional soft magnets are manufactured through industrial processes specifically optimized for magnetic performance, whereas the present study focuses on validating the capability of CEDS to consolidate amorphous powders while largely preserving their microstructure. From this perspective, the magnetic properties achieved are reasonable and comparable to those reported for other powder-based consolidation techniques, confirming that CEDS constitutes a promising route for the fabrication of bulk amorphous or nanocrystalline soft magnetic components with geometrical flexibility.

4. Conclusions

Amorphous ribbons of $Fe_{78}Si_9B_{13}$ were produced at laboratory scale by melt spinning, with an efficiency of 90%. These ribbons achieve a microhardness of 936 ± 15 $HV_{0.1}$, and coercivity, saturation flux density, and remanent flux density of 33 A/m, 0.40 T and 0.24 T, respectively. Elemental analysis confirms an excellent agreement between the nominal and measured compositions, with only minor deviations. Trace amounts of Cu originate from the copper wheel used during melt spinning, while the small oxygen content detected is associated with slight surface oxidation during post-processing handling, a well-known behaviour in Fe–B–rich amorphous alloys.

The ribbons were subjected to mechanical milling for 30 and 120 min, resulting in powders with mean particle sizes of 262 and 65 μm. XRD, TEM and DSC reveal that the powders largely retain the amorphous character, with the finer powder showing the presence of a certain fraction of nanocrystals. Detailed compositional analysis reveals a progressive decrease in the Fe, Si and B contents with milling time, accompanied by a significant increase in oxygen and minor contributions from Cr, Mn, Ni and Cu originated from the equipment wear. This evolution agrees with the oxidation of fresh reactive surfaces during milling in air, which, nevertheless, can contribute to the stabilization of the amorphous matrix.

The electrical sintering process leads to well-consolidated compacts when proper parameters are selected during the capacitors' discharge. Moreover, to obtain highly densified materials, it is necessary to apply an external pressure in the order of the 200 MPa that ensures a good contact of the electrode with the powder column.

The influence of the capacitance on the sintering process is lower than that of the voltage. The use of 1 or 2 capacitors is not particularly critical, although the results are slightly better with 2 capacitors. Furthermore, if the capacitor's charge voltage is the maximum allowed by the equipment, i.e., 200 V, other parameters, such as the powders' particle size, do not hinder achieving good sintering.

Due to the void spaces between sintered particles, and probably to the internal stresses in the compacts, a magnetic hardening of the materials is observed. It is not clear in this research the influence of the appearance of a fraction of α-Fe(Si) nanocrystals, lower than 60%, but they are appearing in an uncontrolled way during the sintering process.

Coercivities of 3415 and 4008 A/m, remanent flux densities of 0.035 and 0.034 T, and saturation flux densities of 1.42 and 1.38 T are achieved in the powders milled for 30 and 120 min.

After sintering, the best magnetic properties are obtained with 1.00 g of powder milled for 30 min (with a mean size of 262 μm) and sintered with 2C and 200 V. The measured coercivity, remanent flux density, and saturation flux density are 1895 A/m, 0.03 T, and 1.32 T, respectively. This compact achieves a porosity of 0.11, a microhardness around 1100 HV_1 and an electrical resistivity of 7.97×10^{-7} Ω·m.

Therefore, this research reveals interesting results in terms of the CEDS technique on materials that need to preserve the structure of the starting material. Other published studies on the Fe-Si-B alloy show that, without stress-relief treatments and annealing for nanocrystallization, the coercivity values are much higher. However, for magnetic applications, the microstructure of these materials still requires to be controlled in the proper way.

Author Contributions: Conceptualization, R.M.A., F.G.C. and J.M.M.; Methodology, R.M.A. and F.G.C.; Validation, R.M.A., J.M.M., P.U. and J.C.; Writing—original draft, R.M.A. and F.G.C.; Writing—review and editing, R.M.A., P.U., J.C., J.M.M. and F.G.C. All authors have read and agreed to the published version of the manuscript.

Funding: This research is part of the R&D&I project PID2021-123750-OB-I00, funded by MICIU/AEI/10.13039/501100011033/and by "ERDF A way of making Europe". Funding for experimental analyses: EPIT2024 University of Huelva, Spain.

Data Availability Statement: The raw data supporting the conclusions of this article will be made available by the authors on request.

Acknowledgments: The authors also wish to thank the technicians C. Cantero and C. Lara (University of Huelva, Spain), and M. Sánchez, J. Pinto, C. Cerrillo, S. Medina and F. Varela (University of Seville, Spain), for experimental assistance.

Conflicts of Interest: The authors declare no conflicts of interest. The funders had no role in the design of the study; in the collection, analyses, or interpretation of data; in the writing of the manuscript, or in the decision to publish the results.

References

1. Inoue, A.; Hashimoto, K. *Amorphous and Nanocrystalline Materials: Preparation, Properties, and Applications*, 1st ed.; Springer: Berlin/Heidelberg, Germany, 2001.
2. Soni, P.R. *Mechanical Alloying: Fundamentals and Applications*; Cambridge Int Science Publishing: Cambridge, UK, 2000.
3. Lavernia, E.J.; Srivatsan, T.S. The rapid solidification processing of materials: Science, principles, technology, advances, and applications. *J. Mater. Sci.* **2010**, *45*, 287–325. [CrossRef]
4. Berger, S.A.; Ai, D.K. A simple fluid mechanical model for planar flow casting melt-spinning. *Metall. Trans. B* **1988**, *19*, 571–579. [CrossRef]
5. Zheng, Q.; Hu, H.; Li, M.; Tao, X.; Gu, J.; Wang, T.; Li, Z. Rapidly solidified amorphous and microcrystalline phases by laser glazing. In Proceedings of the International Conference on Lasers and Optoelectronics SPIE, Bejing, China, 1–31 October 1993.
6. Koziel, T.; Pajor, K.; Gondek, L. Cooling rate evaluation during solidification in the suction casting process. *J. Mater. Res. Technol.* **2020**, *9*, 13502–13508. [CrossRef]
7. Ray, R.; Giessen, B.C.; Grant, N.J. New non-crystalline phases in splat cooled transition metal alloys. *Scr. Metall.* **1968**, *2*, 357–359. [CrossRef]
8. Lu, Y.; Huang, Y.; Wu, J. Laser additive manufacturing of structural-graded bulk metallic glass. *J. Alloys Compd.* **2018**, *766*, 506–510. [CrossRef]

9. Zallen, R. Models of amorphous solids. *J. Non-Cryst. Solids* **1985**, *75*, 3–14. [CrossRef]
10. Egami, T.; Dmowski, W.; Ryu, C.W. Medium-Range Order Resists Deformation in Metallic Liquids and Glasses. *Metals* **2023**, *13*, 442. [CrossRef]
11. Kim, Y.H.; Inoue, A.; Masumoto, T. Ultrahigh Mechanical Strengths of $Al_{88}Y_2Ni_{10-x}M_x$ (M = Mn, Fe or Co) Amorphous Alloys Containing Nanoscale fcc-Al Particles. *Mater Trans. JIM* **1991**, *32*, 599–608. [CrossRef]
12. Wang, Q.; Yang, Y.; Jiang, H.; Liu, C.T.; Ruan, H.H.; Lu, J. Superior Tensile Ductility in Bulk Metallic Glass with Gradient Amorphous Structure. *Sci. Rep.* **2014**, *4*, 4757. [CrossRef]
13. Zhang, X.; Zhao, C.; Xiao, C.; Yuan, Z.; Huang, J. Superplastic Forming of Zr-Based Bulk Metallic Glasses. *Metals* **2024**, *14*, 18. [CrossRef]
14. Li, X.S.; Su, F.C.; Zhou, J.; Mao, Y.C.; Yang, J.M.; Xue, Z.Y.; Ke, H.B.; Sun, B.A.; Wang, W.H.; Bai, H.Y. Ductile Fe-based amorphous alloy with excellent soft magnetic properties induced by low-temperature stress annealing. *Intermetallics* **2024**, *166*, 108201. [CrossRef]
15. Chae, W.S.; Li, M.W.; Cao, Q.P.; Wang, X.D.; Ding, S.Q.; Zhang, D.X.; Jiang, J.Z.; Caron, A. Excellent corrosion and wear resistance of amorphous and crystalline ZrCoAl alloys. *J. Alloys Compd.* **2023**, *968*, 172055. [CrossRef]
16. Li, L.; Qian, Y.; Wang, Z.; Tong, Q.; Wang, M.; Pan, Q.; Yu, Y. Research Progress on the Corrosion Behavior of Metallic Glass and Its Composites. *Metals* **2025**, *15*, 1345. [CrossRef]
17. Kruzic, J.J. Bulk Metallic Glasses as Structural Materials: A Review. *Adv. Eng. Mater.* **2016**, *18*, 1308–1331. [CrossRef]
18. Bobadilla, R.D.B.; Baricco, M.; Palumbo, M. Machine Learning-Driven Prediction of Glass-Forming Ability in Fe-Based Bulk Metallic Glasses Using Thermophysical Features and Data Augmentation. *Metals* **2025**, *15*, 763. [CrossRef]
19. Inoue, A.; Takeuchi, A.; Shen, B. Formation and functional properties of Fe-based bulk glassy alloys. *Mater. Tran* **2001**, *42*, 970–978. [CrossRef]
20. Ponnambalam, V.; Poon, S.J.; Shiflet, G.J. Fe-based bulk metallic glasses with diameter thickness larger than one centimeter. *J. Mater. Res.* **2004**, *19*, 1320–1323. [CrossRef]
21. Ma, R.; Yu, P. The influences of matrix materials on the magnetic and mechanical properties of $Fe_{78}Si_{13}B_9$ soft magnetic composites fabricated by injection molding. *Mater. Res. Bull.* **2021**, *139*, 111256. [CrossRef]
22. German, R.M. *Powder Metallurgy Science*; Metal Powder Industries Federation: Princeton, NJ, USA, 1984.
23. Ma, H.; Qin, D.; Shang, C.; Lu, Y. Laser Additive Manufacturing of Layered Zr-Based Bulk Metallic Glass Composite. *Metals* **2023**, *13*, 986. [CrossRef]
24. Mahbooba, Z.; Thorsson, L.; Unosson, M.; Skoglund, P.; West, H.; Horn, T.; Rock, C.; Vogli, E.; Harrysson, O. Additive manufacturing of an iron-based bulk metallic glass larger than the critical casting thickness. *Appl. Mater. Today* **2018**, *11*, 264–269. [CrossRef]
25. Erutin, D.; Popovich, A.; Sufiiarov, V. Selective Laser Melting of (Fe-Si-B)/Cu Composite: Structure and Magnetic Properties Study. *Metals* **2023**, *13*, 428. [CrossRef]
26. Li, C.; Chen, J.; Hou, S.; Zhang, Q.; Li, X.; Kou, S. Effects of spark plasma sintering parameters on properties of Fe-based bulk amorphous alloys. *Mater. Today Commun.* **2023**, *37*, 107068. [CrossRef]
27. Zhang, D.W.; Zhang, Y.; Cai, Y.F.; Zang, B.W.; Zhao, F.; Wang, Y.C.; Umetsu, R.; Li, Z.Z.; Tong, X.; Huo, J.T.; et al. Magnetic properties evaluation of Fe-based amorphous alloys synthesized via spark plasma sintering. *J. Non-Crystall. Solids* **2023**, *613*, 122373. [CrossRef]
28. Shivakumar, S.; Keyu, C.; Huang, W.; Luo, J. Induction ultrafast sintering. *Scr. Mater.* **2026**, *272*, 117066. [CrossRef]
29. Montes, J.M.; Cuevas, F.G.; Ternero, F.; Astacio, R.; Caballero, E.S.; Cintas, J. Medium-Frequency Electrical Resistance Sintering of Oxidized C.P. Iron Powder. *Metals* **2018**, *8*, 426. [CrossRef]
30. Montes, J.M.; Cuevas, F.G.; Cintas, J.; Urban, P. A One-Dimensional Model of the Electrical Resistance Sintering Process. *Metall. Mater. Trans. A* **2015**, *46*, 963–980. [CrossRef]
31. Urban, P.; Ternero, F.; Caballero, E.S.; Nandyala, S.; Montes, J.M.; Cuevas, F.G. Amorphous Al-Ti powders prepared by mechanical alloying and consolidated by electrical resistance sintering. *Metals* **2019**, *9*, 1140. [CrossRef]
32. Aranda, R.M.; Ternero, F.; Lozano-Pérez, S.; Montes, J.M.; Cuevas, F.G. Capacitor electrical discharge consolidation of metallic powders—A Review. *Metals* **2021**, *11*, 616. [CrossRef]
33. Aranda, R.M.; Ternero, F.; Aranda, B.; Montes, J.M.; Cuevas, F.G. Low-Voltage Capacitor Electrical Discharge Consolidation of Iron Powder. *Metals* **2022**, *12*, 1461. [CrossRef]
34. Aranda, R.M.; Astacio, R.; Urban, P.; Aranda, B.; Cuevas, F.G. Milling amorphous FeSiB ribbons with vibratory ball and disc mill. *Powder Technol.* **2024**, *441*, 119816. [CrossRef]
35. Yurlova, M.S.; Demenyuk, V.D.; Lebedeva, L.Y.; Dudina, D.V.; Grigoryev, E.G.; Olevsky, E.A. Electric pulse consolidation: An alternative to spark plasma sintering. *J. Mater. Sci.* **2014**, *49*, 952–985. [CrossRef]
36. Fais, A.; Maizza, G. Densification of AISI M2 high speed steel by means of capacitor discharge sintering (CDS). *J. Mater. Process. Technol.* **2008**, *202*, 70–75. [CrossRef]

37. Forno, I.; Actis Grande, M.; Fais, A. On the application of Electro-sinter-forging to the sintering of high-karatage gold powders. *Gold. Bull.* **2015**, *48*, 127–133. [CrossRef]
38. Fais, A. Processing characteristics and parameters in capacitor discharge sintering. *J. Mater. Process. Technol.* **2010**, *210*, 2223–2230. [CrossRef]
39. Fais, A. A faster FAST: Electro-Sinter-Forging. *Mater. Today* **2018**, *73*, 80–86. [CrossRef]
40. An, Y.B.; Oh, N.H.; Chun, Y.W.; Kim, Y.H.; Park, J.S.; Choi, K.O.; Eom, T.G.; Byun, T.H.; Kim, J.Y.; Hyun, C.Y.; et al. Surface characteristics of porous titanium implants fabricated by environmental electro-discharge sintering of spherical Ti powders in a vacuum atmosphere. *Scr. Mater.* **2005**, *53*, 905–908. [CrossRef]
41. Ghavimi, A.; Chegeni, M.R.; Ruschel, L.; Adam, B.; Rodríguez-Sánchez, M.; Pérez-Prado, M.T.; Gallino, I.; Busch, R. Assessment of the Fe-Si-B eutectic composition using calorimetry and microstructural analysis. *Mater. Today Commun.* **2026**, *51*, 114741. [CrossRef]
42. Nachnani, A.; Li-Caldwell, K.K.; Biswas, S.; Sharma, P.; Ouyang, G.; Singh, P. Interpretable machine learning-guided design of Fe-based soft magnetic alloys. *Phys. Rev. Mater.* **2025**, *9*, 084411. [CrossRef]
43. Inoue, A.; Kong, F. *Soft Magnetic Materials. Encyclopedia of Smart Materials*, 1st ed.; Olabi, A.G., Ed.; Elsevier: Amsterdam, The Netherlands, 2022; Volume 1, pp. 10–23.
44. Aranda, R.M.; Astacio, R.; Ternero, F.; Urban, P.; Cuevas, F.G. Structure and size distribution of powders produced from melt-spun Fe-Si-B ribbons. *Key Eng. Mater.* **2021**, *876*, 25–30. [CrossRef]
45. *ISO 6507-1: 2018*; Metallic Materials—Vickers Hardness Test—Part 1: Test Method. International Organization for Standardization: Vernier, Switzerland, 2018.
46. MPIF. MPIF Standard 42. Method for Determination of Density of Compacted or Sintered Powder Metallurgy (PM) Products Materials. In *Standard Test Methods for Metal Powders and Powder Metallurgy Products*; MPIF—Metal Powder Industries Federation: Princeton, NJ, USA, 2022.
47. Uhlir, A.J. The potentials of infinite systems of sources and numerical solutions of problems in semiconductor engineering. *Bell Syst. Tech. J.* **1955**, *34*, 105–128. [CrossRef]
48. Xia, Y.; Chen, Y.; Qin, X.; He, L.; Dong, B.; Lan, S. Surface oxidation of FeSiB amorphous alloy and its effect on metallic glass fiber reinforced cement mortar. *Sci. Rep.* **2025**, *15*, 36346. [CrossRef]
49. Fiedler, H.; Mühlbach, H.; Stephani, G. The effect of the main processing parameters on the geometry of amorphous metal ribbons during planar flow casting (PFC). *J. Mater. Sci.* **1984**, *19*, 3229–3235. [CrossRef]
50. Gao, H.; Li, Z.; Zhou, S.; Zhang, G.; Cui, N. The improvement of surface quality and thickness stability of $Fe_{78}Si_9B_{13}$ melt-spun ribbons by melt overheating. *Prog. Nat. Sci. Mater. Int.* **2019**, *29*, 556–560. [CrossRef]
51. Kulik, T.; Latuszkiewicz, J.; Matyja, H. Effect of ribbon dimensions on the magnetic properties of metallic glasses. *Mater. Sci. Eng. A* **1991**, *133*, 236–240. [CrossRef]
52. Sun, X.; Cabral-Prieto, A.; Yacaman, M.J.; Reyes-Gasga, J.; Hernandez Reyes, R.; Morales, A.; Sun, W. Nanocrystallization behavior and magnetic properties of amorphous $Fe_{78}Si_9B_{13}$ ribbons. *Phys. B Condens. Matter* **2000**, *291*, 173–179. [CrossRef]
53. Gleiter, H. Materials with ultrafine microestructures: Retrosprectives and perspectives. *Nanostruc. Mater.* **1992**, *1*, 1–19. [CrossRef]
54. Tumanski, S. *Handbook of Magnetic Measurements*; CRC Press: Boca Raton, FL, USA, 2016.
55. Bansal, C.; Fultz, B.; Johnson, W.L. Crystallization of Fe-B-Si metallic glass during ball milling. *Nanostruct. Mater.* **1994**, *4*, 919–925. [CrossRef]
56. Suryanarayana, C. Mechanical alloying and milling. *Prog. Mater. Sci.* **2001**, *46*, 1–184. [CrossRef]
57. Zhang, C.; Zhang, Z.; Qi, Z.; Qi, Y.; Zhang, J.; Bian, X. Ball milling induced abnormal crystallization behavior of an amorphous $Fe_{78}Si_9B_{13}$ alloy. *J. Non-Crys. Solids* **2008**, *354*, 3812–3816. [CrossRef]
58. Kaptás, D.; Kemény, T.; Balogh, J.; Bujdosó, L.; Kiss, L.F.; Pusztai, T.; Vincze, I. Magnetic properties of melt-quenched amorphous $Fe_2(B_{1-y}Zr_y)$. *J. Phys.: Condens. Matter* **1999**, *11*, L65.
59. Gupta, P.; Gupta, A.; Franco, V.; Conde, A. Joule heating as a technique for obtaining uncoupled soft and hard magnetic phases in a Finemet alloy. *J. Appl. Phys.* **2007**, *101*, 033909. [CrossRef]
60. Trudeau, M.L.; Dignard-Bailey, L.; Schulz, R.; Dussault, D.; Van Neste, A. Fabrication of nanocrystalline iron-based alloys by the mechanical crystallization of amorphous materials. *Nanostr. Mater.* **1993**, *2*, 361–368. [CrossRef]
61. Suryanarayana, C. In situ mechanical crystallization of amorphous alloys. *J. Alloys Compd.* **2023**, *961*, 171032. [CrossRef]
62. Greer, A.L. Metallic Glasses. *Science* **1995**, *267*, 1947–1953. [CrossRef]
63. Tong, Y.; Wang, J.T.; Ding, B.Z.; Jiang, H.G.; Lu, K. The structure and properties of nanocrystalline $Fe_{78}B_{13}Si_9$ alloy. *J. Non-Crystall. Solids* **1992**, *150*, 444–447. [CrossRef]
64. Wang, W.M.; Jin, S.F.; Zhang, J.T.; Huang, T.; Wang, L.; Bian, X.F. Microstructure evolution in the rapidly quenched $Fe_{78}Si_9B_{13}$ ribbons. *Phys. B Condens. Matter* **2009**, *404*, 3413–3416. [CrossRef]
65. Jen, S.U.; Lee, C.Y. Crystallization in amorphous $Fe_{78}B_{13}Si_9$. *J. Magn. Magn. Mater.* **1990**, *89*, 214–220. [CrossRef]
66. Bang, J.Y.; Lee, R.Y. Crystallization of the metallic glass $Fe_{78}B_{13}Si_9$. *J. Mater. Sci.* **1991**, *26*, 4961–4965. [CrossRef]

67. Stoica, M.; Roth, S.; Eckert, J.; Schultz, L.; Baró, M.D. Bulk amorphous FeCrMoGaPCB: Preparation and magnetic properties. *J. Magn. Magn. Mater.* **2005**, *290–291*, 1480–1482. [CrossRef]
68. Zeng, Q.; Baker, I.; McCreary, V.; Yan, Z. Soft ferromagnetism in nanostructured mechanical alloying FeCo-based powders. *J. Magn. Magn. Mater.* **2007**, *318*, 28–38. [CrossRef]
69. Taghvaei, A.H.; Stoica, M.; Khoshkhoo, M.S.; Thomas, J.; Vaughan, G.; Janghorban, K.; Eckert, J. Microstructure and magnetic properties of amorphous/nanocrystalline $Co_{40}Fe_{22}Ta_8B_{30}$ alloy produced by mechanical alloying. *Mater. Chem. Phys.* **2012**, *134*, 1214–1224. [CrossRef]
70. Lin, Z.H.; Dai, D.S. A theory of internal stress field and configuration of magnetic domain in amorphous ribbons. *J. Magn. Magn. Mater.* **1983**, *31–34*, 1540–1542. [CrossRef]
71. Tejedor, M.; Garcia, J.A.; Carrizo, J.; Elbaile, L. Mechanical determination of internal stresses in as-quenched magnetic amorphous metallic ribbons. *J. Mater. Sci.* **1997**, *32*, 2337–2340. [CrossRef]
72. Armyanov, S.; Vitkova, S.; Blajiev, O. Internal stress and magnetic properties of electrodeposited amorphous Fe-P alloys. *J. Appl. Electrochem.* **1997**, *27*, 185–191. [CrossRef]
73. Zbroszczyk, J.; Ciurzynska, W.; Wyslocki, B.; Szymura, S.; Swierczek, J.; Rasek, J.; Baran, M.; Narita, K. Magnetic properties of amorphous ribbons after surface and heat treatment. *J. Magn. Magn. Mater.* **1992**, *112*, 313–314. [CrossRef]
74. Ri, M.C.; Ding, D.W.; Sun, B.A.; Wang, J.Q.; Zhu, X.S.; Wang, B.B.; Wang, T.L.; Qiu, Q.Q.; Huo, L.S.; Wang, W.H. Stress effects on magnetic property of Fe-based metallic glasses. *J. Non-Crystall. Solids* **2018**, *495*, 54–58. [CrossRef]
75. Herzer, G. Soft magnetic nanocrystalline materials. *Scr. Metall. Mater.* **1995**, *33*, 1741–1756. [CrossRef]
76. Jo, Y.H.; Kim, Y.H.; Jo, Y.J.; Seong, J.G.; Chang, S.Y.; Reucroft, P.J.; Kim, S.B.; Lee, W.H. Self-Consolidation Mechanism of Porous-Surfaced Ti Implant Compacts Induced by Electro-Discharge-Sintering of Spherical Ti Powders. *Met. Mater. Int.* **2015**, *21*, 337–344. [CrossRef]
77. Chang, S.Y.; Jang, H.S.; Yoon, Y.H.; Kim, Y.H.; Kim, J.Y.; Lee, Y.K.; Lee, W.H. Self-consolidation and surface modification of mechanical alloyed Ti-25.0 at.% Al powder mixture by using an electro-discharge technique. *Arch. Met. Mater.* **2017**, *62*, 1293–1297. [CrossRef]
78. Kim, C.K. Effects of crystallization on the coercivity in $Fe_{78}Si_9B_{13}$ amorphous alloy. *Mater. Sci. Eng. B* **1996**, *39*, 195–201. [CrossRef]
79. Ohta, M.; Yoshizawa, Y. Recent progress in high Bs Fe-based nanocrystalline soft magnetic alloys. *J. Phys. D Appl. Phys.* **2011**, *44*, 064004. [CrossRef]
80. Larimian, T.; Chaudhary, V.; Khan, M.U.F.; Ramanujan, R.V.; Gupta, R.K.; Borkar, T. Spark plasma sintering of Fe–Si–B–Cu–Nb / Finemet based alloys. *Intermetallics* **2021**, *129*, 107–135. [CrossRef]
81. Larimian, T.; Chaudhary, V.; Christudasjustus, J.; Ramanujan, R.V.; Gupta, R.; Borkar, T. Bulk-nano spark plasma sintered Fe-Si-B-Cu-Nb based magnetic alloys. *Intermetallics* **2020**, *124*, 106–869. [CrossRef]
82. Lu, W.; Yan, B.; Tang, R. Bulk metglas, finemet and nanoperm soft magnetic alloys prepared by ultra-high-pressure consolidation. *J. Alloys Compd.* **2006**, *425*, 406–410. [CrossRef]